

ID-FAST - Investigations on degradation mechanisms and Definition of protocols for PEM Fuel cells Accelerated Stress Testing

Grant agreement no: 779565

Call: H2020-JTI-FCH-2017-1

D3.1: Report on models describing the main degradations modes and analysis of their stressing factors

Authors:	T. Jahnke, P. Sarkezi-Selsky (DLR) G. Serre (CEA) A. Bisello, A. Baricci (POLIMI)
Confidentiality	PUBLIC
First issue date	03.04.2019
Submission date	29.08.2019



Summary

This deliverable contains a description of the degradation models developed in the first period of the project ID-FAST as well as the simulation results. Models for all relevant degradation mechanisms occurring in the MEA have been developed:

- A detailed catalyst degradation model is used to investigate the effect of potential cycling for different AST protocols as well as for two driving cycles.
- A carbon corrosion model is adopted to study the degradation occurring during start and stop.
- A simplified and a more detailed membrane degradation model are presented to investigate the effect of iron ion and hydrogen peroxide concentration on membrane degradation.
- A Lattice Boltzmann model is developed to investigate the effect of PTFE-degradation on the flooding behaviour of the GDL.

Revisions

Version	Date	Author(s) (partner)	Comments (<i>inputs added, revision, approval...</i>)
1	03.04.2019	T. Jahnke (DLR)	Draft provided
2	08.07.2019	T. Jahnke, P. Sarkezi-Selsky (DLR)	DLR contributions added
3	09.07.2019	G. Serre (CEA)	CEA contribution added
4	19.07.2019	A. Bisello, A. Baricci (POLIMI)	POLIMI contribution added
5	22.07.2019	T. Jahnke (DLR)	Contributions merged
6	21.08.2019	A. Baricci (POLIMI)	Minor revisions
Final	29.08.2019	S. Escribano (CEA)	Final submission



Contents

1. Introduction.....	4
2. Catalyst degradation model	5
3. Carbon corrosion model	16
4. Membrane degradation model	32
5. GDL degradation model.....	52
References	60



D3.1: Report on models describing the main degradations modes and analysis of their stressing factors



1. Introduction

This deliverable summarizes the status of the degradation model development in the ID-Fast project. ID-Fast deals with the development of accelerated stress test (AST) protocols for PEMFC as well as with the quantification of transfer functions from “real world operation” to AST operation and vice versa. The developed models should help in understanding the occurring degradation mechanisms and the stressors in order to provide a theoretical basis for the AST development.

2. Catalyst degradation model

2.1. Model description

The degradation model for the catalyst is based on the model developed in the EU project Second Act and has been further improved by including an additional platinum dissolution mechanism due to the reduction of platinum oxide as well as the precipitation of platinum ions in the membrane and the consequent platinum band formation as described in the following. In total the catalyst degradation model includes a submodel for the formation and reduction of platinum oxides, the dissolution of platinum, the growth of platinum particles due to Ostwald ripening and the platinum band formation as depicted in Figure 1. In the following the governing equations are briefly described.

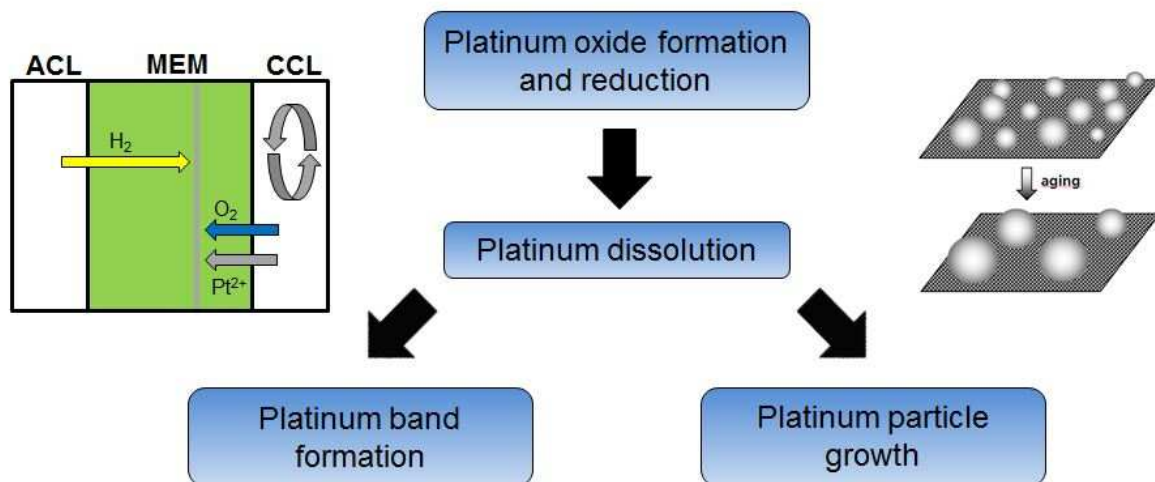


Figure 1: Scheme of the catalyst degradation model

2.1.1. Platinum oxide model

The platinum oxide model consists of a three step mechanism



The reaction rates are calculated according to

$$r_1 = k_1 \left[(1 - \theta_1) a_{H_2O} e^{-\frac{\omega_1 \theta_1}{RT}} e^{\frac{\alpha_1 n_1 F}{RT} \eta_1} - \theta_1 e^{-\frac{(1-\alpha_1) n_1 F}{RT} \eta_1} \right], \quad (4)$$

$$r_2 = k_2 \theta_1 e^{-\frac{\omega_2 \theta_2}{RT}} e^{\frac{\alpha_2 F}{RT} \Delta \Phi}, \quad (5)$$

$$r_3 = k_3 \theta_2 e^{-\frac{\alpha_3 F}{RT} \Delta \Phi}, \quad (6)$$

where θ_1 is the coverage of PtOH and θ_2 the coverage of PtO. All symbols used in these and the following equations of the catalyst degradation model are defined in Table 1.

In Second Act this model has been demonstrated to accurately describe the potential dependent platinum oxide evolution (Second Act D3.4 “Report on local reversible mechanisms with interaction on irreversible degradation and durability validation at single cell level”).

2.1.2. Platinum dissolution model

Two mechanisms for platinum dissolution are considered. The direct dissolution of platinum



which strongly depends on the size of the particles due to the radius dependent surface energy. The dissolution rate is calculated as

$$r_{diss,1} = A(r) \Gamma k_f e^{\frac{-E_a}{RT}} \left[(1 - \theta_1) e^{\frac{(1-\alpha)nF}{RT} \eta_{d1}} e^{\frac{2(1-\alpha)\Omega\gamma}{RT r}} - \frac{k_r}{k_f} c_{Pt^{2+}} e^{-\frac{\alpha n F}{RT} \eta_{d1}} e^{-\frac{2\alpha\Omega\gamma(\theta_1, \theta_2)}{RT r}} \right], \quad (8)$$

Where the surface tension is dependent on the oxide coverage and given by

$$\gamma(\theta_1, \theta_2) = \gamma_0 + \Gamma RT \left[\theta_1 \log(\theta_1) + (1 - \theta_1) \log(1 - \theta_1) - \frac{n_1 F}{RT} \eta_1 \theta_1 + \frac{\omega_1 \theta_1^2}{2RT} + \theta_2 \log(\theta_2) - \theta_2 + \log\left(\frac{k_3}{k_2 \theta_2}\right) \theta_2 - \frac{\alpha_2 + \alpha_3}{RT} F \Delta \Phi \theta_2 + \frac{\omega_2 \theta_2^2}{2RT} \right], \quad (9)$$

The second mechanism is new compared to the model of Second Act and describes the dissolution due to the reduction of platinum oxides according to



This mechanism takes into account that the place exchange between platinum and oxygen atoms can cause the dissolution of the platinum atoms during oxide reduction, i.e., during cathodic potential sweeps, as has been observed experimentally[4, 21]. We assume that this mechanism is also dependent on the particle size due to the size-dependent fraction of edge sites $X_{\text{edge}}(r)$ which



should be more prone to dissolution. Thus, the dissolution rate due to the second mechanism is calculated as

$$r_{diss,2} = A(r)\Gamma k_{f,2} X_{edge}(r) r^3. \quad (11)$$

The radius dependent number of edge sites can be calculated based on the particle geometry. For cuboctahedron type particles it is given by[15]

$$X_{edge} = \frac{12 + 24(n_{edge} - 2)}{6(n_{edge} - 2)^2 + 4(n_{edge} - 3)(n_{edge} - 2) + 12 + 24(n_{edge} - 2)}, \quad (12)$$

with the number of atoms along the edge

$$n_{edge} = \left[\frac{4\pi}{\sqrt{50}} \right]^{1/3} \frac{r}{2.77 \cdot 10^{-10}}. \quad (13)$$

2.1.3. Ostwald ripening model

The catalyst particles are described by the local particle size distribution $N(r,t)$ whose time evolution is governed by the balance equation

$$\frac{\partial N(r,t)}{\partial t} + \frac{\partial}{\partial r} \left(N(r,t) \frac{\partial r}{\partial t} \Big|_{Ostwald} \right) = 0, \quad (14)$$

where the change of particle radius due to Ostwald ripening is calculated from the dissolution rates as

$$\frac{\partial r}{\partial t} \Big|_{Ostwald} = \frac{\Omega}{A(r)} (r_{diss,1} + r_{diss,2}). \quad (15)$$

The dissolved platinum ions can move within the ionomer according to the Nernst-Planck equation

$$\frac{d(\phi_{ionomer} c_{Pt^{2+}})}{dt} + \nabla \Phi_{Pt^{2+}} - q_{Pt^{2+}} = 0, \quad (16)$$

where the flux of platinum ions due to concentration and ionic potential gradients is given by

$$\Phi_{Pt^{2+}} = -u_{Pt^{2+}} RT \nabla c_{Pt^{2+}} - 2F u_{Pt^{2+}} c_{Pt^{2+}} \nabla \Phi_{ion}. \quad (17)$$



2.1.4. Platinum band formation

The platinum ions can move from the cathode catalyst layer into the membrane where they can react with the hydrogen coming from the anode side to form the so-called platinum band. This formation can be described by the reaction



The platinum band formation can be considered to consist of two steps, a nucleation step in which platinum particles are formed and a second step in which the ions are deposited on the existing particles leading. The kinetics of both steps can be described as

$$r_{\text{Pt-band},1} = k_{\text{Pt-band},1} c_{\text{Pt}^{2+}} c_{\text{H}_2} \quad (19)$$

$$r_{\text{Pt-band},2} = k_{\text{Pt-band},2} c_{\text{Pt}^{2+}} c_{\text{H}_2} c_{\text{Pt}} \quad (20)$$

For the simulations presented in the following a simplified model with only the first reaction kinetics has been taken into account, while for the coupling with the membrane degradation both reaction steps will be considered.

On the platinum band the combustion of hydrogen with oxygen can take place according to



with the reaction kinetics calculated as

$$r_c = k_c c_{\text{Pt}} c_{\text{H}_2}^2 c_{\text{O}_2} \quad (22)$$

This reaction will change the local concentration of hydrogen in the membrane and therefore affect the further platinum band formation.

The catalyst degradation model has been coupled with the single cell PEMFC model in the DLR modeling framework NEOPARD-X[7] in order to simulate different degradation tests presented in the next section.

Table 1: List of symbols for catalyst degradation model

a_i	Activity of species i / -
$A(r)$	Surface area of particles with radius r / $\text{m}^2 \text{m}^{-3}$
c_i	Concentration of species i / mol m^{-3}



D3.1: Report on models describing the main degradations modes and analysis of their stressing factors



ECSA	Electrochemically active surface area / $\text{m}^2 \text{m}^{-3}$
F	Faraday constant / C mol^{-1}
k_f	Forward rate constant of platinum dissolution reaction / s^{-1}
k_i	Rate constant of platinum oxide reaction i / s^{-1}
$k_{\text{Pt-band},1}$	Rate constant of platinum band formation reaction 1 / $\text{m}^3 \text{mol}^{-1} \text{s}^{-1}$
$k_{\text{Pt-band},2}$	Rate constant of platinum band formation reaction 2 / $\text{m}^6 \text{mol}^{-2} \text{s}^{-1}$
k_c	Rate constant of hydrogen combustion reaction / $\text{m}^9 \text{mol}^{-3} \text{s}^{-1}$
k_r	Backward rate constant of platinum dissolution reaction / s^{-1}
$N(r)$	Particle size distribution / m^{-4}
n_{edge}	Number of platinum atoms along the particle edge / -
n_i	Number of electrons involved in reaction i / -
R	Universal gas constant / $\text{J mol}^{-1} \text{K}^{-1}$
r_i	Volumetric reaction rate of platinum oxide reaction i / s^{-1}
$r_{\text{diss},i}$	Volumetric reaction rate of platinum dissolution reaction i / $\text{mol m}^{-3} \text{s}^{-1}$
$r_{\text{Pt-band},i}$	Volumetric reaction rate of platinum band formation reaction i / $\text{mol m}^{-3} \text{s}^{-1}$
r_c	Volumetric reaction rate of hydrogen combustion reaction / $\text{mol m}^{-3} \text{s}^{-1}$
T	Temperature / K
t	Time / s
$u_{\text{Pt}^{2+}}$	Mobility of platinum ions in ionomer / s mol kg^{-1}
X_{edge}	Fraction of edge sites / -
α_i	Transfer coefficient of reaction i / -
Γ	Site density of platinum / mol m^{-2}
γ	Surface tension / N m^{-1}
γ_0	Surface tension of Pt[111] / N m^{-1}
$\Delta\phi$	Electrode potential / V
θ_i	Coverage of surface species i / -
Φ_{ion}	Ionomer potential / V
Ω	Molar volume of platinum / $\text{m}^3 \text{mol}^{-1}$
ω_i	Interaction parameter of species i / J mol^{-1}

2.2. Results

2.2.1. Simulation of AST protocols

To investigate the effect of potential cycling as stressor for the catalyst degradation, the following AST protocols[10] have been simulated:

- 1) Triangle wave potential cycling between 0.6V and 1.0V (TW)
- 2) Triangle wave potential cycling between 0.6V and 0.85V (TW-LUPL)
- 3) Triangle wave potential cycling with 8 second potential holds at 0.6V and 1.0V (TW-H)
- 4) Square wave potential cycling between 0.6V and 1.0V (SW)

The sweep rate for all triangle waves has been 50mV/s. In all cases the cathode was fed with fully humidified nitrogen, as typically done in catalyst degradation ASTs. The potential cycles are depicted in Figure 2.

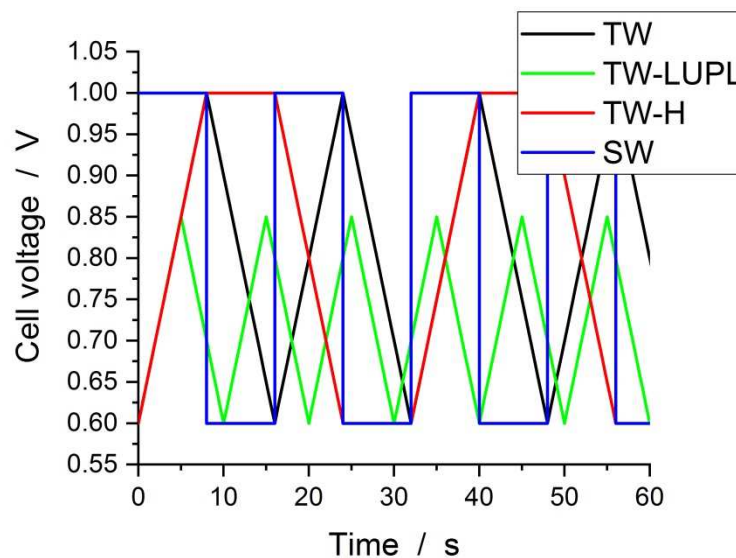


Figure 2: Simulated AST potential cycles

Figure 3 shows the corresponding platinum ion concentrations during the first cycles of these ASTs. Variations of 6 orders of magnitude in ion concentration during the cycles are obtained. The high concentrations during the high potential regions reflect the accelerated degradation during the cycling. In addition a second peak is obtained during the sweep to low potentials which is caused by the dissolution due to reduction of the platinum oxides.

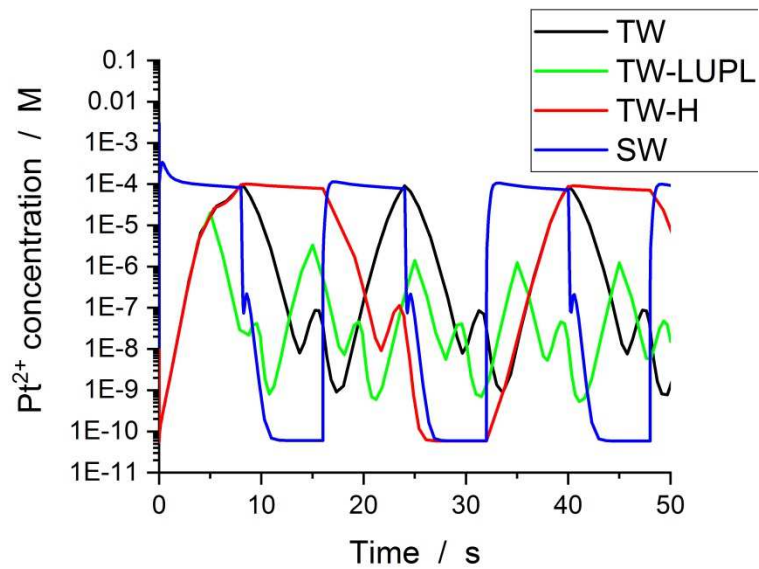


Figure 3: Simulated ion concentrations during the AST potential cycles

The corresponding ECSA losses for the different AST tests are shown in Figure 4 together with the experimental data for the TW AST obtained in the Second Act project. It can be seen that the TW-LUPL protocol leads to the lowest degradation (ECSA loss about 5-6 times lower compared to TW protocol) as expected due to the lower maximum potential and therefore lower platinum dissolution. Instead, the TW-H and SW show the highest ECSA loss, which is about a factor of 2 higher than in the TW case. These trends are in good agreement with the experimental findings[10]. For comparison we also include the simulated ECSA loss for steady-state operation at 0.2A/cm². To make the simulation comparable a “cycle duration” of 16s has been defined for the steady-state which is similar to the cycle duration of the TW and SW AST. It can be seen that the steady-state aging is significantly lower than for the ASTs. This shows that cycling to high potentials is a stressor for the catalyst degradation and is well described by the model.

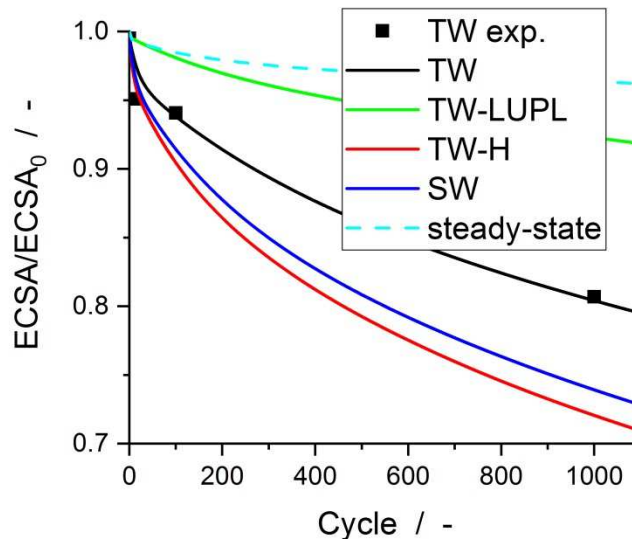


Figure 4: Comparison of ECSA loss for the different AST protocols

As platinum precipitates into the membrane and forms a platinum band, the amount of platinum in the catalyst layer is reduced. This is an additional mechanism leading to ECSA loss in addition to the Ostwald ripening. In order to analyse the contribution of this mechanism to the overall catalyst degradation Figure 5 shows the correlation between platinum loss and ECSA loss in the cathode catalyst layer. Interestingly, the obtained behaviour is quite different for the ASTs compared to steady state operation as the ASTs lead to a significantly higher platinum loss per ECSA loss. The enhanced platinum deposition in the membrane can be attributed to two effects: in case of the ASTs the missing oxygen leads to a deposition of the platinum directly at the membrane-catalyst layer interface while the platinum band is moved towards the anode if oxygen is present at the cathode (cf. Figure 6). Furthermore, the gradients of electrolyte potential are significantly lower for the ASTs while higher gradients under normal operation prevent the platinum ions from moving into the membrane.

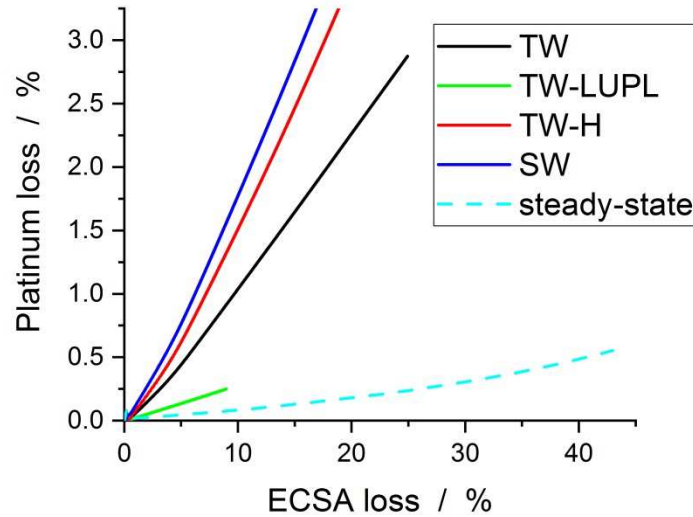


Figure 5: Correlation between platinum loss and ECSA loss in the cathode catalyst layer for the different degradation tests

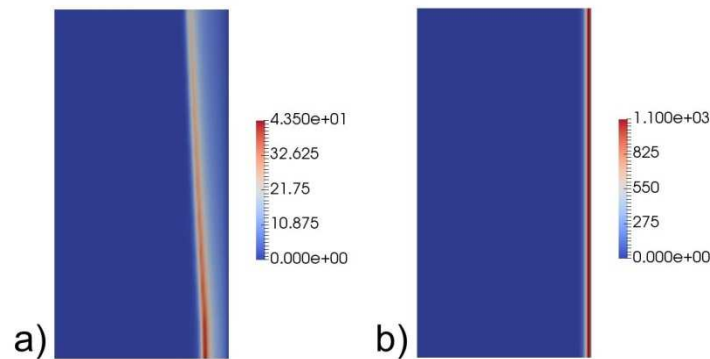


Figure 6: Simulated platinum metal concentration in mol m^{-3} after 25% ECSA loss for a) the steady state operation in air and b) the triangle wave AST. The cathode side is on the right, gas inlet on the top (co-flow). For visualization purposes the figures are scaled by a factor of 10^4 in x-direction.

2.2.2. Simulation of driving cycles

The model was also used to simulate the degradation during the ID-FAST load cycle (cf. D1.1 “Agreed upon test program for ageing tests of SoA-components”) and to compare it with the fuel cell dynamic driving cycle (FC-DLC) proposed by JRC[22]. The load profiles of both driving cycles are shown in Figure 7. To make both cycles comparable the other operating conditions are the same for both cases and listed in Table 2. Note, that a constant temperature is considered during the ID-Fast cycle. The additional stressor of a temperature ramp is not taken into account in this simulation.

Table 2: Operating conditions for the driving cycle simulations

Pressure anode	1.5 bar
Pressure cathode	1.5 bar
Relative humidity anode	100%
Relative humidity cathode	100%
Temperature	80°C
Stoichiometry anode	1.5
Stoichiometry cathode	2.0

The ID-Fast driving cycle is three times longer compared to the FC-DLC and does not include the short OCV periods. The corresponding simulated voltage response is depicted in Figure 8, in particular cell voltages of almost 1V are obtained during the short OCV periods in the FC-DLC, while the highest cell voltage during the ID-Fast driving cycle is about 0.85V.

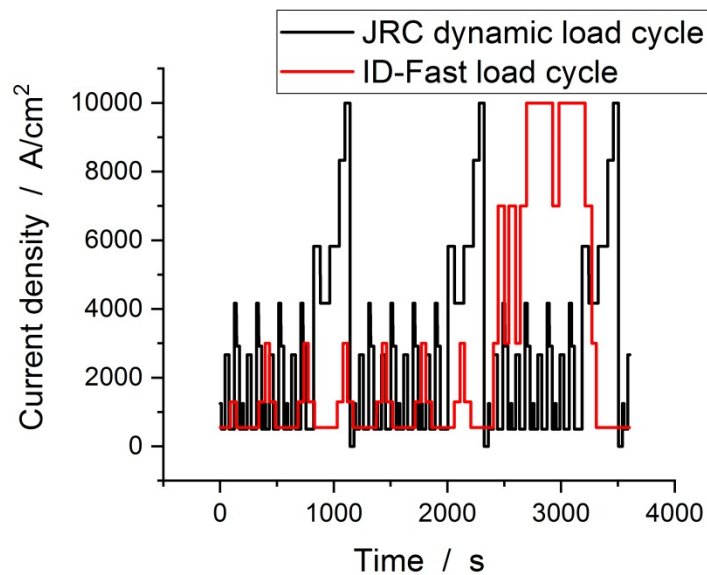


Figure 7 Load profile for ID-Fast load cycle and FC-DLC

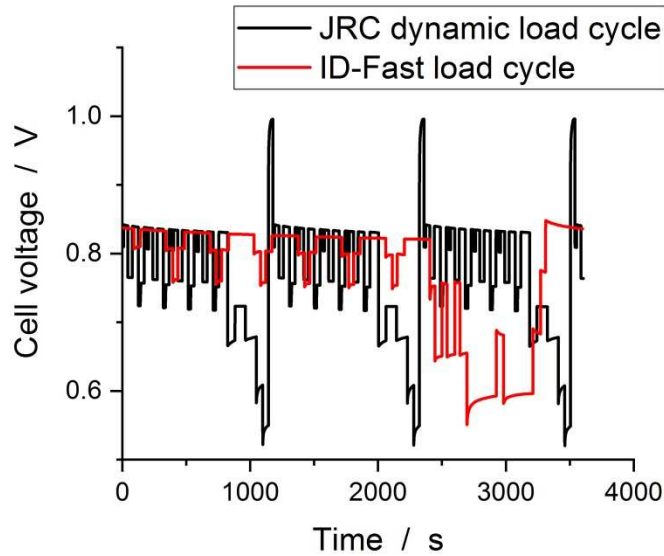


Figure 8 Simulated cell voltage during the driving cycles

The simulated ECSA loss for both driving cycles is compared in Figure 9. According to the simulation we expect higher catalyst degradation for the FC-DLC due to the stressors of OCV periods and faster potential cycling. The inset shows a magnification of the ECSA evolution which clearly shows the accelerated degradation during the short OCV periods in the FC-DLC.

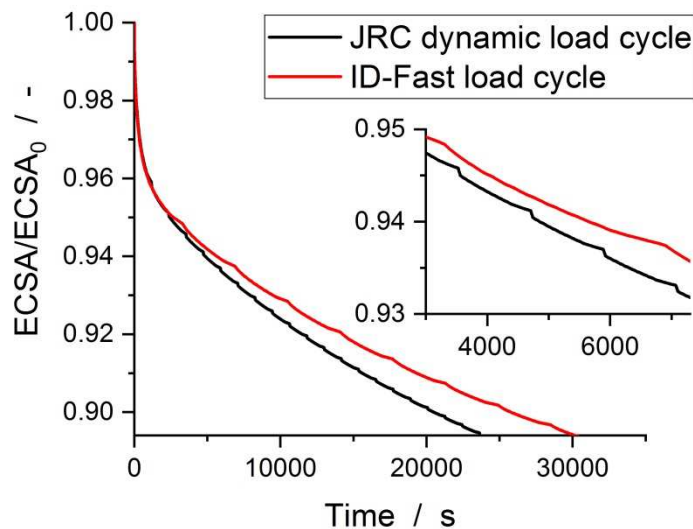


Figure 9 Simulated ECSA loss for both driving cycles



2.3. Conclusions on the catalyst degradation model

A detailed catalyst degradation model including platinum oxidation, dissolution, Ostwald-ripening and platinum band formation has been developed. This model has been used to investigate potential cycling as main stressor for the catalyst degradation. The model correctly describes the experimentally observed accelerated degradation during potential cycling which is caused by the periodic oxidation and reduction of the platinum. Based on the model the highest degradation per time is observed for square wave cycling, while the highest degradation per cycle is observed for the triangle wave with potential holding and the square wave cycling. Even though the potential cycling protocols with nitrogen at the cathode side are very effective in accelerating the ECSA loss, the model also shows that the degradation under these AST protocols behaves quite differently from the one under normal operation. In particular the AST protocols cause an enhanced platinum deposition within the membrane close to the cathode catalyst layer due to the absent oxygen. This suggests that AST protocols with oxygen present would be desirable for a more realistic degradation.

The model was also used to compare the ID-Fast load cycle with the fuel cell dynamic driving cycle (FC-DLC) proposed by JRC. The simulations show an enhanced degradation for the FC-DLC due to the additional OCV periods and the overall more pronounced potential cycling.

3. Carbon corrosion model

A degradation model of carbon corrosion is implemented specifically aiming at providing insight into the dynamics of start-up and shut-down events. In this section, the model is first described (3.1) and then results are presented: the simulation of the reference case is discussed (3.2), then stressing factors are analysed (3.3) and conclusions are discussed (3.4).

3.1. Model description

A 2D transient model was developed in order to study the reverse-current mechanism that occurs under start-up/shut-down operating conditions for a PEMFC, as depicted in Figure 10. The solved domain is divided into five regions that simulate both anode and cathode electrodes: anodic and cathodic gas diffusion layers (GDL's), anodic and cathodic catalyst layers (CL's) and the polymer membrane (PEM).

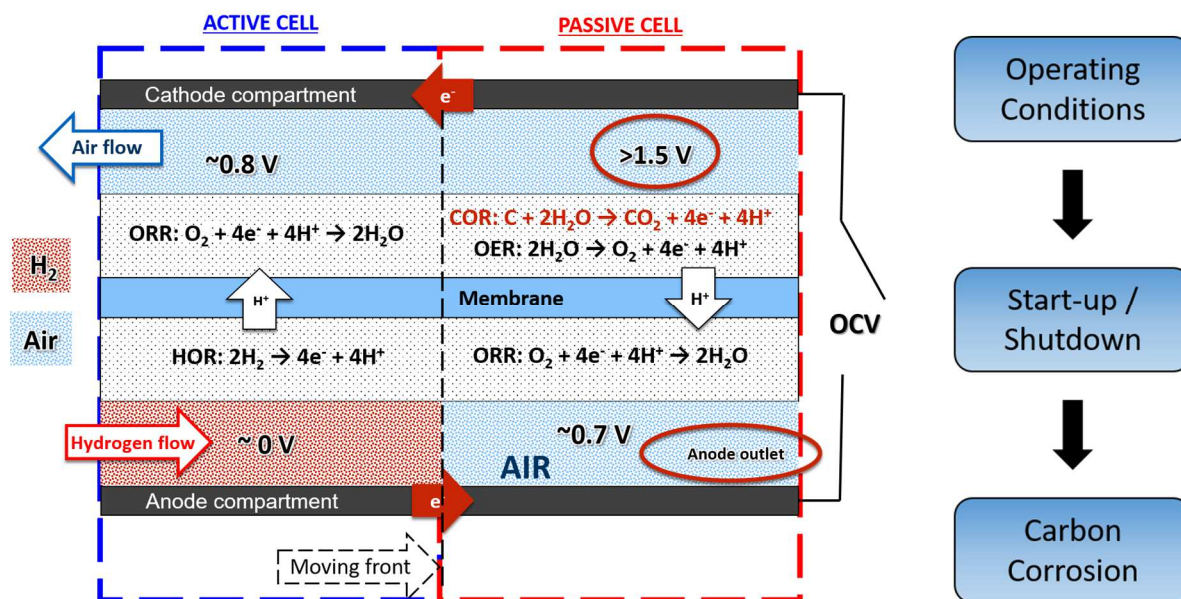


Figure 10 - Scheme of start-up / shutdown process as simulated

Conservation equations for mass and charge are implemented in each layer, along with phenomenological equations to provide a physical description of mass and charge transport. The hydrogen oxidation reaction (HOR, Eq. I) and oxygen reduction reaction (ORR, Eq. II) occur in the anode active layers while oxygen reduction/evolution reactions (ORR/OER, Eq. II) and carbon oxidation reaction (COR, Eq. III) occur in the cathode active layer:



The model relies on the following assumptions:

- I. Local effects over the MEA surface are considered in two major coordinates: along the channels of the gas distributor and through the active layers. Additional 3D effects, *e.g.* gas flow under the ribs of the gas distributor, are neglected in this specific geometry.
- II. Liquid water transport and energy conservation are not solved, neglecting the blocking effect of liquid water on species transport and heating of porous media.
- III. Conservation of water in the ionomer phase is not solved, thus water transport across polymer membrane is neglected and ionic conductivity is calibrated as a constant parameter; this condition is consistent with the fully humidified state that is set in the experiment.
- IV. Pseudo-capacitive currents due to platinum oxidation/reduction are neglected.

Assumptions (II) and (III) are consistent with fast dynamic response that is investigated in this work (simulations focus in the time frame of processes that last < 1 s). The model is described in the following subsections and it is adopted to simulate both steady state operation (polarization curves for model calibration) and the transient response (cyclic voltammetry and start-up/shut-down operation).

3.1.1. Transient 2D model equations

Within each region conservation equations are solved for three phases: gas phase, electron conducting solid phase (indicated with subscript S), ion conducting ionomer or membrane phase (indicated with subscript I). The model implements the conservation equations for each phase, *i.e.* ion conservation (Eq. 23), electron conservation (Eq. 24), gas species conservation (Eq. 25):

$$\nabla \cdot \mathbf{j}_s = - \sum_m \mathbf{nF} \cdot \mathbf{r}_m - C_{DL} \frac{d(\varphi_S - \varphi_I)}{dt} \quad (23)$$

$$\nabla \cdot \mathbf{j}_I = \sum_m \mathbf{nF} \cdot \mathbf{r}_m + C_{DL} \frac{d(\varphi_S - \varphi_I)}{dt} \quad (24)$$

$$\nabla \cdot \mathbf{N}_i = - \sum_m \mathbf{v}_i \cdot \mathbf{r}_{i,m} - \varepsilon \frac{dC_i}{dt} \quad (25)$$

The source terms (\mathbf{r}) are present in the anode and cathode catalyst layers and represent the rate of the electrochemical reaction: source terms are zero in the equations (Eq. 23-25) in the GDL and polymer membrane. Phenomenological equations that represent the transport phenomena and link the fluxes to gradient of potentials are included to close the physical problem, in particular Ohm's law for ion and electron transport (Eq. 26 and 27), Fick's law of diffusion for mass transport (Eq. 28):

$$\mathbf{j}_S = -\sigma_S \cdot \nabla \varphi_S \quad (26)$$

$$\mathbf{j}_I = -\sigma_I \cdot \nabla \varphi_I \quad (27)$$

$$\mathbf{N}_i = -\frac{\varepsilon}{\tau} \cdot \mathbf{D}_i^F \cdot \nabla C_i \quad (28)$$

Diffusion coefficients and conductivities in Eq. 26-28 are effective properties that are corrected for porosity and tortuosity of the medium; reaction rate is represented by Butler-Volmer equation for ORR/OER, Tafel law for COR and linearized Butler-Volmer equation is adopted for HOR:

$$\mathbf{r}_{HOR} = \mathbf{i}_{0,HOR} \text{ECSA} \cdot \mathbf{a}_{H_2} \left(\frac{(\alpha_O + \alpha_R) \cdot F}{R \cdot T} \right) \cdot (\varphi_S - \varphi_I - E_{eq}) \quad (29)$$

$$\mathbf{r}_{BV} = \mathbf{i}_{0,BV} \text{ECSA} \left[\mathbf{a}_O \exp \left(\frac{\alpha_O \cdot F \cdot (\varphi_S - \varphi_I - E_{eq})}{R \cdot T} \right) - \mathbf{a}_R \cdot \exp \left(-\frac{\alpha_R \cdot F \cdot (\varphi_S - \varphi_I - E_{eq})}{R \cdot T} \right) \right] \quad (30)$$

3.1.2. Geometry and Model Parameters

Consistently with the model description, the solved domain consists of seven parts, to study both anode and cathode channels, gas diffusion layers (GDLs), catalyst layers (CLs) and the polymeric membrane. A single straight channel which length was set to 50 mm is simulated. The size of the channel was selected based on a compromise between physical accuracy and computational effort: a longer channel would have requested more memory usage and longer computational time, without improving much the representativeness of the simulation (geometry is reported in Figure 11).

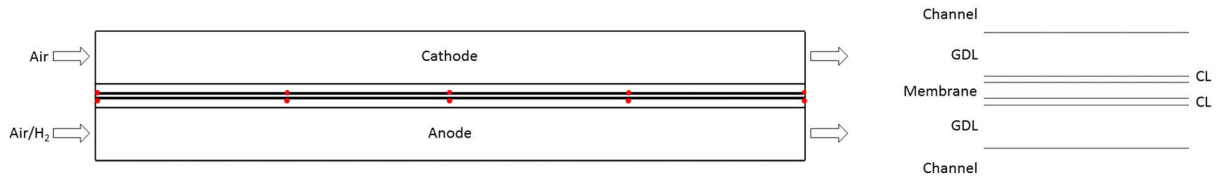


Figure 11 – (a) Geometrical description of the domain. (b) Layout zoom of MEA layers

Anode and cathode electrodes are considered symmetrical, consistently with the properties of the preliminary materials adopted in the experimental activity (as reported in WP4). The geometrical parameters of the domains and the material and transport properties are summarized in Table 3.

A rectilinear grid mapped mesh was used, which was regularly distributed along the channel direction and non-uniform through cell direction, getting finer from the channel to the polymeric membrane, to ensure a proper discretization of the thin catalyst layers and the membrane. Probe points have been implemented on the interface between CLs and GDLs along the channel length (at start, 1/4, 1/2, 3/4, end of the channel, see Figure 11) to mimic the measurement performed with the local reference hydrogen electrodes (RHEs), obtained in Task 4.2.

Table 3: – (a) Geometrical parameters for reference case

Parameter	Symbol	Value
Channel Length	L_{ch}	50 mm
Channel Height	d_{ch}	0.8 mm
GDL Height	d_{GDL}	135 μm
GDL Porosity	$\epsilon_{p,GDL}$	0.6
GDL Tortuosity	τ_{GDL}	4
CL Height	d_{CL}	20 μm
CL Porosity	$\epsilon_{p,CL}$	0.4
CL Tortuosity	τ_{CL}	9
Membrane Height	d_{MEM}	50 μm

(b) Transport properties

Parameter	Symbol	Value
Electric conductivity GDL	$\sigma_{s,GDL}$	10^7 S m^{-1}
Electric conductivity CL	$\sigma_{s,CL}$	10^2 S m^{-1}
Ionic conductivity CL	$\sigma_{i,CL}$	2.459 S m^{-1}



Ionic conductivity PEM	$\sigma_{I, MEM}$	2.459 S m^{-1}
H ₂ Diffusivity	D_{H_2}	$5 \cdot 10^{-5} \text{ m}^2 \text{ s}^{-1}$
O ₂ Diffusivity	D_{O_2}	$1 \cdot 10^{-5} \text{ m}^2 \text{ s}^{-1}$
N ₂ Diffusivity	D_{N_2}	$1 \cdot 10^{-5} \text{ m}^2 \text{ s}^{-1}$
H ₂ O Diffusivity	D_{H_2O}	$1 \cdot 10^{-5} \text{ m}^2 \text{ s}^{-1}$

(c) Kinetics parameters

HOR		ORR		OER		COR	
$i_{0, HOR}$	$0.3 \text{ A cm}_{Pt}^{-2}$	$i_{0, ORR}$	$2.47 \cdot 10^{-5} \text{ A cm}_{Pt}^{-2}$	$i_{0, OER}$	$1.89 \cdot 10^{-9} \text{ A cm}_{Pt}^{-2}$	$i_{0, COR}$	$1.03 \cdot 10^{-18} \text{ A cm}_{Pt}^{-2}$
E^0_{HOR}	0 V	E^0_{ORR}	1.2291 V	E^0_{OER}	1.2291 V	E^0_{COR}	0.2073 V
E^{act}_{HOR}	10 KJ mol^{-1}	E^{act}_{ORR}	67 KJ mol^{-1}	E^{act}_{OER}	38 KJ mol^{-1}	E^{act}_{COR}	134 KJ mol^{-1}
ΔE_{HOR}	0 V K^{-1}	ΔE_{ORR}	$-0.8456 \cdot 10^{-3} \text{ V K}^{-1}$	ΔE_{OER}	$-0.8456 \cdot 10^{-3} \text{ V K}^{-1}$	ΔE_{COR}	$-0.853 \cdot 10^{-3} \text{ V K}^{-1}$
$\alpha_a + \alpha_c$	1	α_c	0.5	α_a	0.12	α_c	0.67

(c) Material properties in the reference case

Parameter	Symbol	Value
Catalyst active surface	$ECSA_{Pt}$	$65 \text{ m}^2 \text{ g}^{-1}$
Pt loading	L_{Pt}	$0.3 \text{ mg}^2 \text{ cm}^{-2}$
Carbon active surface	$ECSA_c$	$800 \text{ m}^2 \text{ g}^{-1}$
Pt/C ratio	$r_{Pt/C}$	$0.75 \text{ g}_{Pt} \text{ g}_C^{-1}$
Double layer capacitance	C_{dl}	25 F m^{-2}

3.2. Model Validation

Different operating conditions were simulated to clarify their effects on the aging mechanisms. In particular, the model permits to simulate the contribution of the different faradic and capacitive currents to distinguish the carbon corrosion current and elucidate the acceleration (named stressors in the next) or mitigation effect of the operating conditions on the corrosion of the carbon support. Firstly, the stressors were analysed: oxygen dilution (at anode / cathode compartment), hydrogen dilution during start-up, temperature, and gas flow rate (also reported in literature such as residence time effect). The model was also used to simulate the combined effect the different degradation mechanisms such as: platinum dissolution, catalysts layer thinning, and others different mechanisms which contribute to increase the mass-transport resistance. The last task, on the simulation of

combined mechanisms is not reported here, where instead the stressors effects have been widely treated.

3.2.1. Start-up and shut-down simulations: description of the process and comparison with experiments

Figure 12 (left) reports the experimental measurement local potential with RHE under shut-down and Figure 12 (right) the experimental measurement of local potential with RHE under start-up, which is used here for comparison against simulations (data collected in Task 4.2): during open circuit condition under H_2 /air, the anode side is at the equilibrium potential of 0 V versus hydrogen electrode, thus cathodic voltage is around 0.9 V, that is the cell open circuit voltage (OCV).

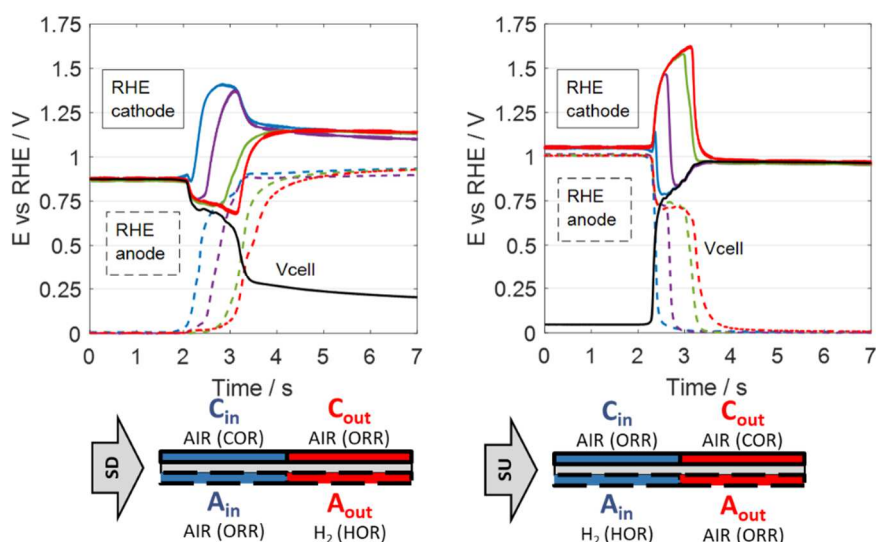


Figure 12 – Local potential measured with RHE in Task 4.2 during shut-down (left) and start-up (right).

Potential profiles obtained at $T = 40^\circ\text{C}$, $RH = 100\%$; mass flows: $air_{cathode} = 200 \text{ ml min}^{-1}$, $air_{anode} = H_{2,anode} = 100 \text{ ml min}^{-1}$, $p_{out} = 1 \text{ atm}$. Position of each RHE is specified by the schematic representation in Figure 11, while black curve is the cell voltage.

As the gas is switched from hydrogen to air during SD (Figure 12 left), the cell voltage, represented in black, drops rapidly. The voltage of cathode inlet increases, while cathode outlet goes down. Indeed, the anode outlet is filled with H_2 thus it operates as a fuel cell (active), that is the ORR at the cathode and HOR at the anode. The inlet instead is affected by the air front, that forces down the electrolyte potential causing a high cathodic potential seen by cathode and operates as an electrolyte (passive), that is ORR at the anode and COR/OER at the cathode. Initially, almost all the anode is active and operates under HOR as the front gets inside and progressively switches to ORR: such transition is highlighted by a variation in concavity of the anode potential and in the slope of potential raise in time. At the end of the shut-down, the whole anode volume is filled with air: voltage is around 0 V, but it takes a very long time, and all the reference electrodes measure a potential between 1 V - 1.1

V, suggesting an equilibrium condition with oxygen in air. Hydrogen is then introduced to simulate start-up in Figure 12 (right). The process is symmetric to shut-down in the experimental procedure and it is found that the cathodic outlet is now in the passive region, characterized by high potential values. Cathodic inlet instead operates with ORR: note that since the measured point is not really at the entrance of the channel, a transition from passive to active operation is here visible (which was not visible under shut-down). All the anodic potentials go down while the cell comes back to H₂/air OCV. Nevertheless, the results of start-up and shut-down are not symmetric: first of all, the duration of start-up is lower; second, the shape of the potential profile is not the same, which is observed both for anode and cathode and cathode potential shows even larger peak values than shut-down.

In order to get insights about the circulating currents and to support the conclusion drawn from the experimental tests, a numerical simulation of the SUSD process is presented in Figure 13.

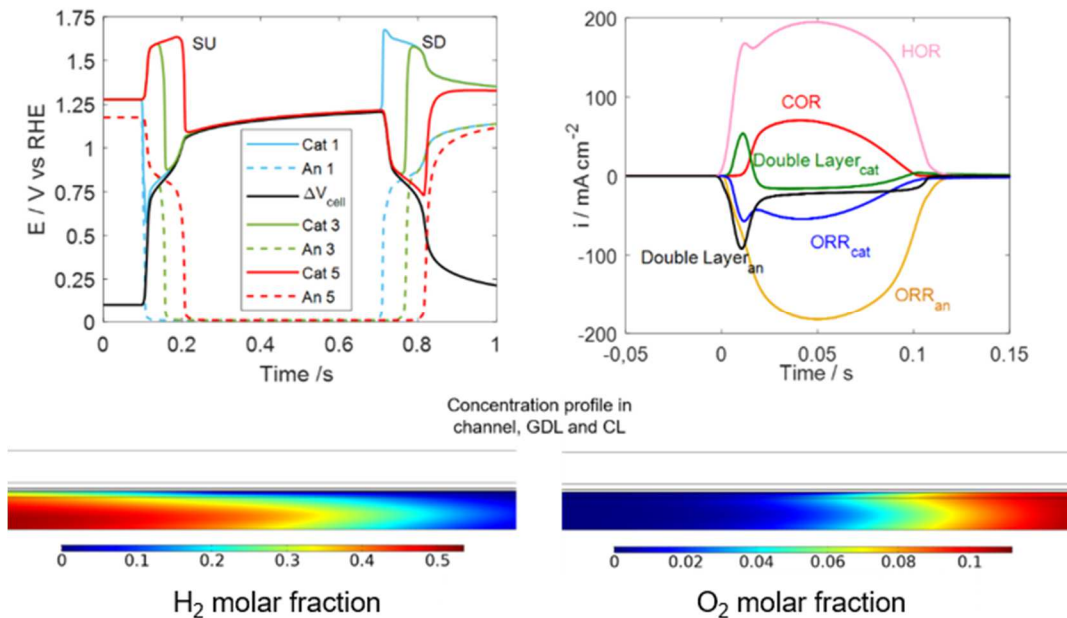


Figure 13 – Left) Simulated potentials of cathode and anode in probe positions 1, 3 and 5 (positions in Figure 11) during start-up and shut-down; Right) Simulated global currents during start-up integrated over the whole cell surface; Bottom) Simulated concentration of hydrogen (left) and oxygen (right) during the start-up process. The images are taken at $t = 0.14$ s and both represent the same relevant portion of the domain, from $x = 11$ mm to $x = 24$ mm (length channel 50 mm).

First of all, potential profiles provided by the model and reported in Figure 13 (left) approximately match with experiments, providing a general consistency between model and experiment. Main differences are consequence of the real geometry and of 3D effects: in particular ribs/bends which cause mass flow alterations with respect to 2D geometry, which can impact the result. During start-up, cathode inlet generates a very high local current because it supplies the entire remaining MEA, which works as passive. Indeed, while the first portion of the cell is fed with hydrogen and is active, all the rest is under oxygen and acts as passive, then becomes successively active once in presence of



H₂ front. During shut-down, the potential peak shows a different shape which is later discussed in relation with capacitive effects in Section 3.2.2. The first cell segment produces the highest COR current and is sustained by the rest of the domain which works as a fuel cell. Figure 13 (right), makes evident the weight of capacitive currents due to double layer occurring in the transient: capacitance gives its contribution whenever electrode potential increases or decreases. The difference in time scale between model and experiments is instead due to the different residence time (or channel length) considered in the two cases, as discussed in Section 3.1.

The rest of the analysis is mainly focusing on start-up, which is more relevant from a technological point of view, considering that several mitigation strategies exist for shut-down. Under SU, a fast rise in cell potential is observed initially and, according to the integral currents reported in Figure 13 (right), the cathode electrode sustains the process by, initially, double-layer capacitive currents during potential rise, until potential is high enough to have carbon corrosion current maintaining the process. Note that, for sake of simplicity, oxygen evolution reaction is not depicted in the chart because of its almost negligible contribution at 80°C, as obtained from simulation. When hydrogen reaches the active site, instead, it shifts rapidly down the local anode electrode potential, therefore anode capacitance generates a negative anodic current which sums up to anodic ORR. The cathode electrode at the position where the H₂/air front is located, switches from passive (COR) to active operation (ORR). Since the reverse current circulating across the cell progressively fades, as expected from the moment that the passive region becomes smaller as the front proceeds, the local cathode potential of the active region raises towards OCV and the capacitive current changes from positive to negative until leading, in the end, to a current flowing in the opposite direction. The concentration of the reactants in time and space is also studied. In Figure 13 (bottom left), it is possible to see how, during SU, the movement of the hydrogen front in the channel is not matched by the hydrogen progress in the catalyst layer, in disagreement with the plug-flow assumption usually used in the literature. The oxygen displacement is also shown in Figure 13 (bottom right); it is visible how the consumption of oxygen in the CL affects the profile of the outgoing oxygen front in the catalyst layer. In Figure 14, the current density associated to carbon corrosion during start-up is split into the contribution of four segments (numbered from 1 to 4) reporting the spatial distribution of the support degradation over the all active surface. It is found that degradation is strongly heterogenous, consistently with the local potential profiles discussed above. In particular, the inlet region (SEG1) is not affected by this degradation mechanism, while the outlet region accounts for about 50% of the degradation occurring.

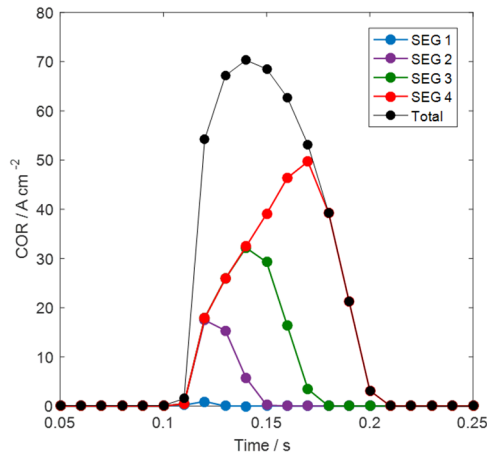


Figure 14 – Current density due to carbon corrosion integrated over the all area (black) and referred to four segments numbered from hydrogen inlet to outlet (SEG1 to SEG4). Each current density is referred to the full active surface.

3.2.2. Double-layer and pseudo-capacitance contribution

Following from previous section, capacitive effects due to both double-layer and pseudo-capacitive currents can significantly influence the charge balance during start-up as well as shut-down. Double-layer capacitance accounts for ion and electron charge distribution at the electrode interface between electrolyte and metal; the model includes both cathode and anode capacitive currents. Pseudo-capacitive currents, instead, come from platinum oxidation/reduction reactions which are affected by electrode potential. At the current state of model development, the contribution of platinum oxides is neglected, because of lack of information on oxide formation in the range 1.0 V – 1.5 V. A first visible effect of capacitive contributions consists in the SU/SD asymmetry of voltage peaks, as already observed in Figure 13 (left). Capacitive current at positive electrode reduces carbon corrosion both during start-up and shut-down because it helps supplying the charge required by the ORR at anode in place of carbon corrosion. The anode capacitance instead plays a different role under start-up or shut-down. During start-up, in fact, the anode potential is reduced (switching from air to hydrogen) thus it sums up to anodic ORR current and is an additional charge flux that requires balancing by cathodic reactions (mostly COR). At the opposite during shut-down, anode potential increases (switching from hydrogen to air), thus ion and electron charge required by anodic ORR are internally supplied at the anode side by capacitive currents. This is the main origin for the lack of symmetry between the local potential profiles during start-up or shut-down, as observed in Figure 13 (left). Figure 15 displays the integral COR and capacitive currents obtained from the simulations during SU and SD: under shut-down (Figure 15 -a), the anodic contribution of double-layer current is consistent with the previous discussion and it shows the same sign of COR, leading to a reduction of COR current compared to start-up (Figure 15-b) where anodic capacitive current increases the support oxidation current. Here cathodic double-layer changes globally its sign from SU-SD, because this current is computed including

both the active and passive part of the cell, which behave differently: as found in Figure 13-a, derivative of potential in time has the opposite sign if considering inlet or outlet local potential.

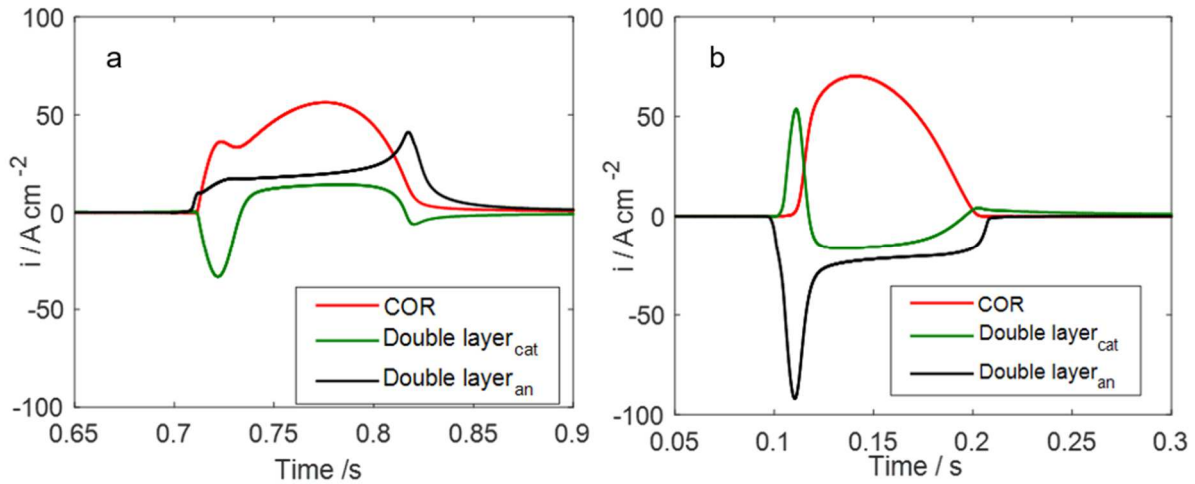


Figure 15 - Simulated global currents during shut down (a) and start-up (b)

3.2.3. Balancing currents

The present analysis of balancing currents is focused on start-up event, but similar conclusions can be drawn from the analysis of shut-down. After SU, when the hydrogen front has passed through the channel, a general charge re-balancing is required, because the cathode electrode potential has different values all over the cell and must equilibrate to a uniform value. The cathode electrode potential of the active part (hydrogen inlet) must increase towards open circuit voltage, while the electrode potential of the passive part (hydrogen outlet) must decrease towards open circuit voltage leading to in-plane electron flow from the inlet to the outlet. Then, potential becomes even all over the electrode domain, and balancing current vanishes. The adjustment necessary to reach the equilibrium state occurs through capacitive contributions, and the results of the simulation are reported in Figure 16-a, where the local current at the outlet is reported. A change in sign of current is observed and graphically explained in scheme of Figure 16-b, in which currents resulting during charge rebalancing are reported in red, which are opposite to the currents previously commented that occur during start-up (blue). Capacitive effects describe the real electrode dynamics. The net effect is that the period at high voltage for cathode is longer in time compared to what expected by the same

mechanism in absence of re-balancing. As confirmed by simulation, the balancing seems to last for about the 25% - 35% of the total process duration.

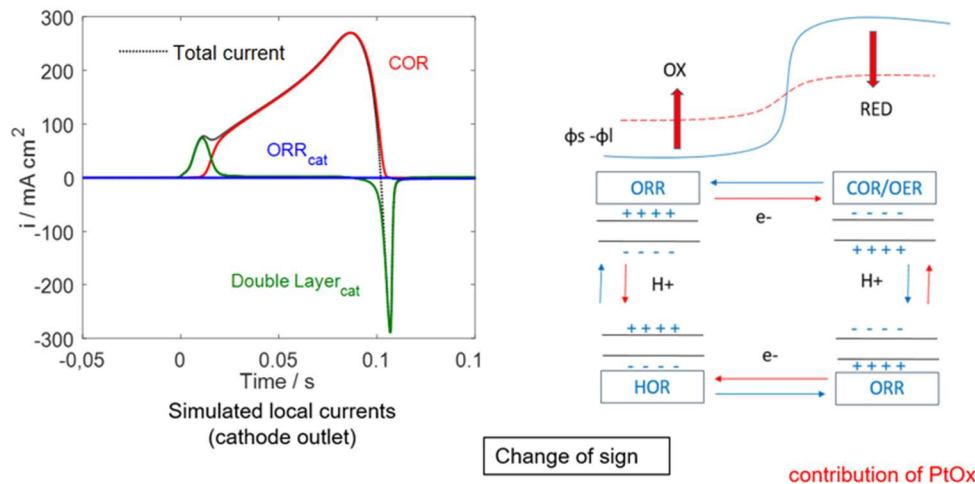


Figure 16 - a) Simulated local currents at cathode outlet; b) balancing mechanism at the end of reverse-current.

3.3. Analysis of Stressors

Stressing factors (or stressors) are analysed to improve the understanding of carbon corrosion degradation mechanism under start-up and shut-down. The analysed stressors are chosen in line with the experimental activity carried out in Task 4.2 and discussed in the following sections: temperature, hydrogen concentration in anode, oxygen concentration in anode, oxygen concentration in cathode.

3.3.1. Stressor 1: Temperature effect

Since the kinetics of electrochemical reactions is strongly influenced by the temperature, this parameter has been necessarily considered when analysing stressors. In the simulation, the effect of the temperature is implemented in the exchange current density with reaction-specific Arrhenius terms. In Figure 17 the experimental results and simulations of start-up performed at low temperature (30/40°C) and 80°C are reported. It is found that a higher cathode peak potential is reached when temperature is lowered, both in experiments and simulations. According to Arrhenius description of temperature dependency of kinetics of COR, it is argued that temperature should reduce exponentially the impact of carbon corrosion. But, during start-up, this effect is opposed to an increase of the local outlet potential as a consequence of the dynamics of the process. The analysis of the potential in the active part of the cathode, where ORR occurs, suggests that current density should increase at high temperature: the lower potential for cathodic ORR during start-up at high



D3.1: Report on models describing the main degradations modes and analysis of their stressing factors



temperature clearly indicates that current of the active region (and consequently of the passive region) is increasing, since kinetic losses are indeed reduced as temperature goes up.

When increasing the temperature, the dry gas flow rates are reduced because relative humidity is unchanged, as was done in the experimental (see Task 4.2), in order to maintain the same residence time. Instead, the partial pressure of hydrogen and oxygen vary significantly when temperature is changed, this should be considered in the physical interpretation of the results. In particular, the oxygen mass in the anode compartment before the start-up increases. This effect, combined with a reduced reverse-current at low temperature, explained the growth of time required to finish the start-up operation. Anyway, to generate a certain current, mainly determined as seen by anodic ORR and thus by anodic oxygen, COR/OER peak changes: as visible from the plots, voltage can raise even though current is lower at a different temperature.

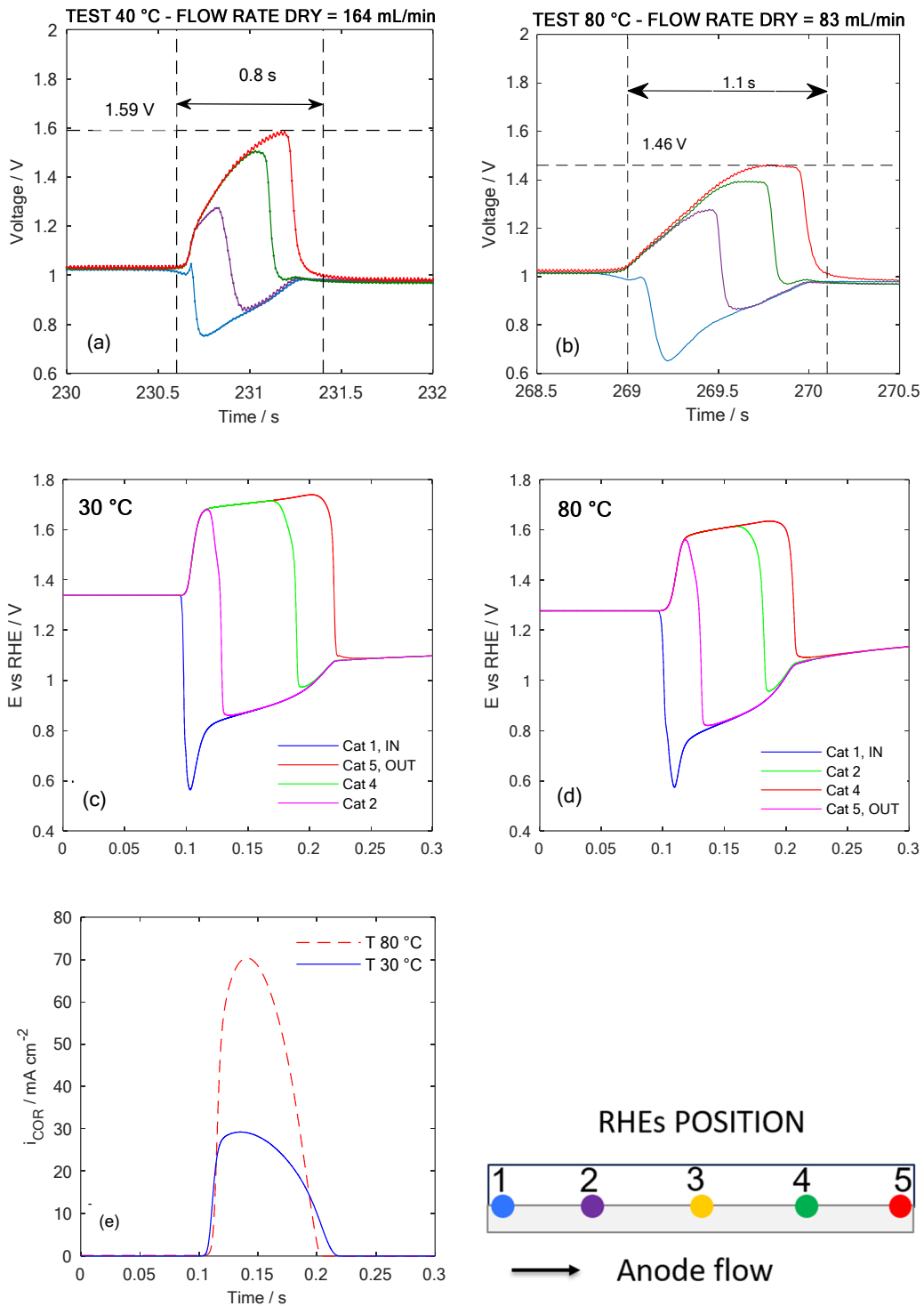


Figure 17 - Analysis of temperature effect. (a-b) Experimental local potential collected with RHEs during start-up at 40°C and 80°C; (c-d) comparison between simulated potential at 30 and 80°C; (e) global current profile simulated at 30 and 80°C

3.3.2. Stressor 2: Oxygen concentration at cathode

A simulation is performed against the reference case, where the oxygen concentration in the cathode compartment is reduced (10.5% dry mole fraction versus air). The main observable effect was a reduction of the total current associate to carbon oxidation reaction, as observed in Figure 18-right. According to the simulation, the total carbon corroded is reduced by 23%, in comparison with the reference case. This effect is mainly attributed to the increase of the ORR overpotential in the active part of the cathode electrode, as visible in Figure 18-left, due to a kinetic effect and/or an increase of the mass-transport loss. As a consequence, the reduction of cathode potential in the active part determines a decrease of the cell voltage (difference between cathode and anode) against the reference case. This results in a reduction of maximum potential of the cathode passive part with a corresponding decrease of carbon corrosion reaction and amount of corroded carbon (see Figure 18-b).

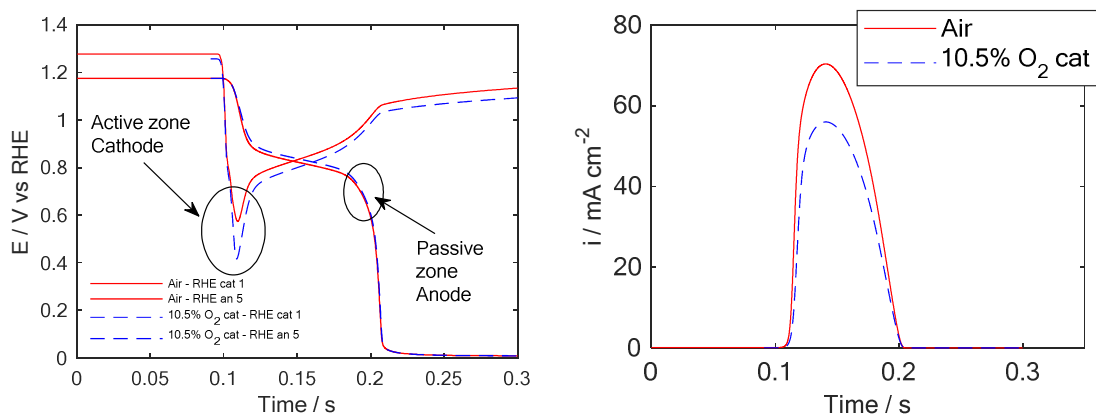


Figure 18 – (left) Comparison between ORR overpotential between active (cathode) and passive (anode) zones; (right) global carbon corrosion current during start-up

3.3.3. Stressor 3: Hydrogen concentration at anode

Hydrogen concentration during start-up was also evaluated to understand the impact of this parameter on the carbon corrosion mechanism. In Figure 19-a the simulated H_2 and O_2 mole fraction profiles are reported during the start-up. The reduction of the hydrogen concentration to 50% (dry gas) limits the diffusion of gas from the channel to the catalyst layer, in comparison with the reference case. A reduction in the reverse-current circulating between active and passive regions is observed because of lower performance of the active region. A decrease of the cathode potential in the passive zone is anyway achieved, as a consequence of a lower cell voltage. The total current flowing during start-up is reduced, but the time required for start-up results enlarged, thus the carbon corroded is only slightly reduced, by 5% with respect to the reference case with 100% H_2 .

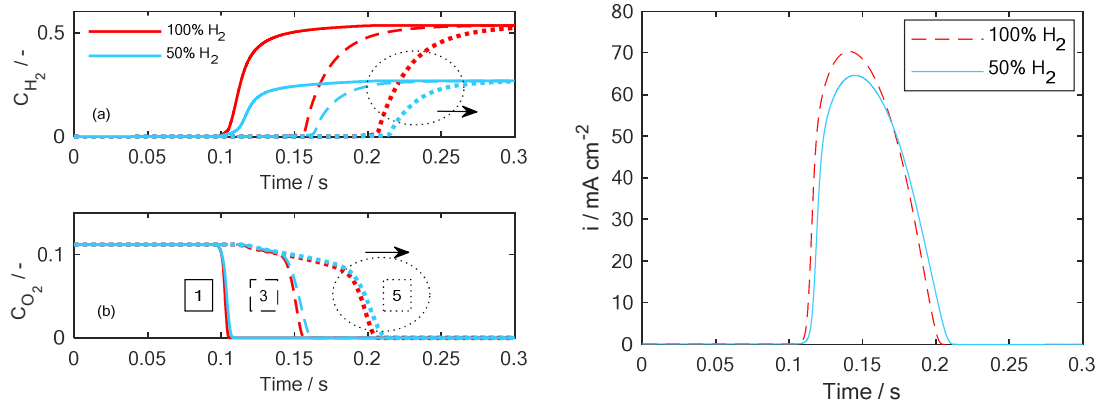


Figure 19 - (a) H₂/O₂ concentration profile in the anode CL during start-up; (b) Comparison between ORR overpotential between active (cathode) and passive (anode) zones.

3.3.4. Stressor 4: Oxygen concentration at anode

The model is also applied to simulate several oxygen concentrations initially present in the anode channel, GDL and CL before start-up. Simulations and experiments are compared in Figure 20. The collected experimental profile, at high oxygen concentration (50% O₂) in the dry gas, shows an increase of the duration of the start-up, an increase in the value of peak potential in the cathode passive zone and a decrease of the minimum potential observed in the cathode active zone. The same trend is well reproduced by the simulation, as visible in Figure 20-b. Here, it is also visible the increase of the potential at the anode in the passive zone under high oxygen concentration. The local potential suggests that high concentration of oxygen causes an increase of the total current flowing due to the reverse-mechanism, boosting carbon corrosion.

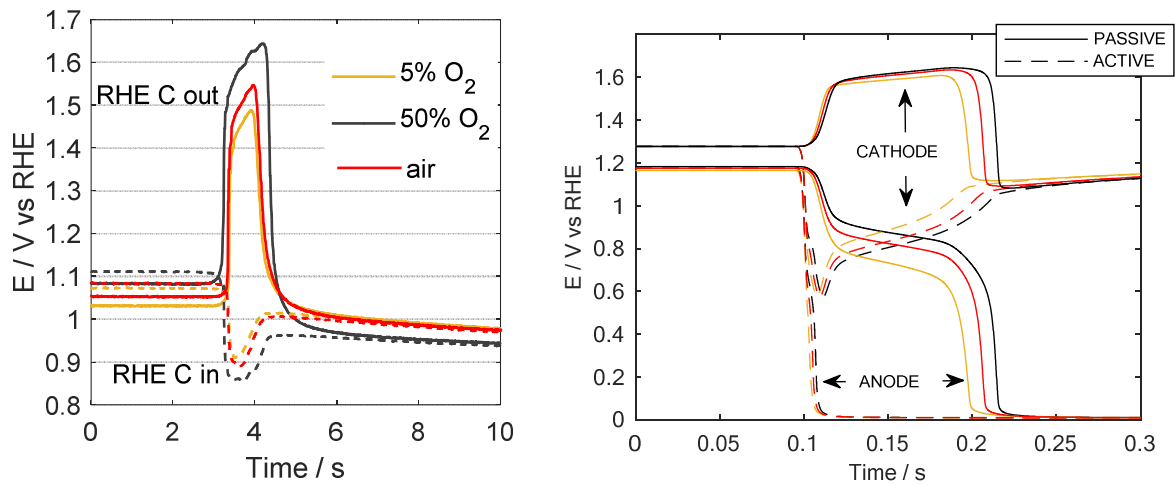


Figure 20 - (a) experimental cathode potentials measured at different oxygen concentration at anode-side; (b) Comparison with simulated profiles.

A better explanation of the contribution of this stressor could be obtained looking at the current profile simulated in Figure 21. The global COR current, reported in Figure 21-a, highlights the fundamental contribution of the anode in the passive zone to control the start-up mechanism. Decreasing the oxygen concentration, the reverse-current is strongly mitigated, lowering at the same time the total carbon corroded. Furthermore, the simulation done at very low oxygen concentration has revealed the basic role played by the capacitive phenomena during start-up. As shown in in Figure 21-b, by nitrogen feeding in the anode compartment, the anodic ORR in the passive zone was switched off. Though anodic ORR was removed in the passive part of the cell, the reverse-current mechanism is fed by capacitive currents due to anodic double-layer. In that case, carbon corrosion current was reduced at 20% with respect to the air feeding.

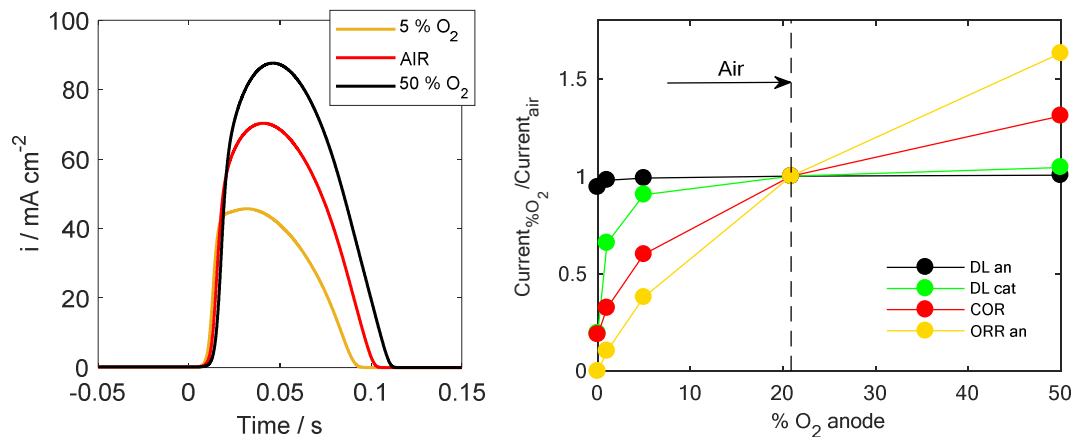


Figure 21 - (a) Simulated COR at different oxygen dilution during Start-up; (b) Comparison between global currents during Start-up simulation at different Oxygen concentrations.

3.4. Conclusions on the start-up /shut-down model

In summary, the simulations highlight that carbon corrosion during start-up/shutdown operation is mainly controlled by the equilibrium between the passive cell and the active cell, in particular the mass of oxygen present in the anode limits the circulating current due to the reverse-current mechanism; regarding the active cell, ORR kinetics affects the potential difference between anode and cathode thus determining the COR current. Furthermore, the stressing factors (stressors) that are already known regarding the carbon corrosion mechanism itself were investigated under transient operation that characterizes start-up/shut-down, highlighting the impact of mitigation strategies, *e.g.* reducing the temperature and reactant concentrations, as commonly done in automotive systems. This analysis indicates that the impact of mitigation strategies (*e.g.* keep low temperature, increase residence time, etc.) is not linearly predicted by the analysis of the impact of single parameters on carbon corrosion reaction rate (*e.g.* temperature, potential), since complex system dynamics occur during start-up that affects the value of cathode potential.



4. Membrane degradation model

4.1. Introduction to the CEA code

CEA uses the MePHYSTO environment [17] from the MUSES platform. This code is a lump parameter model, developed under the Matlab/Simulink software. This model is based on the bond graph theory and it includes model for physics and electrochemistry at the cell level: 1D or 2D convection along bipolar plate channels, 1D multiple gases diffusion through GDL, 1D liquid permeation through GDL, semi-empirical law or Butler-Volmer law in the 0D catalyst layer, 1D motion of proton, liquid and gases through the membrane. When the electrochemical law is used, its parameters are fitted using experimental polarization curves. The temperature field is calculated in each components thanks to 1D diffusion and conduction through plane.

Several irreversible degradation models are available in this code: membrane degradation (see further), platinum dissolution (Oswald ripening), and also reversible degradation models (liquid water flooding, liquid freezing, nitrogen stratification).

Compared to CFD codes, MePHYSTO uses coarse meshing since its physics is modelled at macroscopic scale. Therefore, the CPU time of many simulations is quite small: it is possible to simulate hundreds or thousands of physical hours in a feasible time. Therefore, it is the appropriate code for AST simulations.

In the frame of the project, 2 membrane degradation models have been implemented in MePHYSTO:

- A semi-empirical model developed at CEA [3]
- A Fenton model developed at CEA and Aalborg University [6].

In the next paragraph, we describe these models and we give some validation elements. The validation will continue as new experimental data becomes available.

Only 1 of these 2 models will be used for ageing and AST simulations: the choice will be a compromise between the accuracy, the CPU cost and the ease to couple it with other mechanism degradation models. This choice has not been done yet.

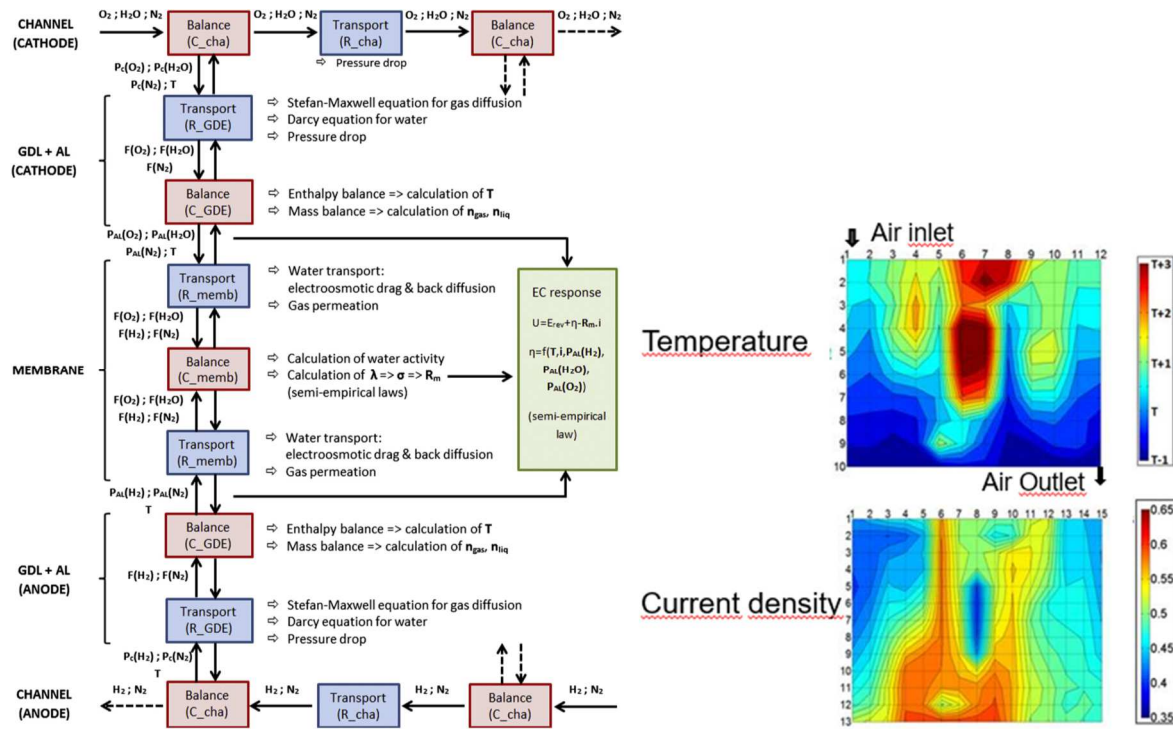


Figure 22: Structure of MePHYSTO - Examples of MePHYSTO results for serpentine geometry (from Robin PhD work and [17])

4.2. Membrane degradation models description

Semi-empirical model

This model has been developed at CEA [3]. It has been derived using data from the Puma Mind European project and considering the membrane chemical degradation mechanism of LaConti [11]. In this model the fluoride release rate (FRR) writes:

$$v_{F^-} = A_1 \underbrace{\frac{\Delta P_{O_2}}{P_0}}_1 \underbrace{\frac{e_M^0}{e_M}}_2 \exp\left(\frac{\alpha_{eq} F}{R T} U\right) \exp\left(-\frac{E_a}{R} \left(\frac{1}{T} - \frac{1}{T_0}\right)\right) \quad (31)$$

Where:

- v_{F^-} (mg/h/cm²) is the FRR,
- P_0 is a reference pressure (10⁵ Pa), ΔP_{O_2} (Pa) is the differential oxygen partial pressure at the inlet of the cell (calculated by the code),
- e_M^0 is the initial membrane thickness (m) and e_M the current membrane thickness (m),
- F (C/mol) is Faraday's constant, R (J/K/mol) is the perfect gas constant,
- T (K) is the cell temperature, T_0 is a reference temperature fixed arbitrarily to 95+273.15K



- U (V) is the cell voltage (calculated by the code),
- $\alpha_{eq} = 0.54$ is an equivalent transfer coefficient
- Ea (J) is an activation energy
- $A1 = 1.7 \cdot 10^{-7}$ mg/h/cm² is the adjustable constant fitted from the experimental data.

The first term of the model expresses, in a nondimensional way, a linear dependence of the membrane degradation with the oxygen crossover. It is based on the oxygen crossover flux that is proportional to the oxygen partial pressure gradient through cell and assuming that membrane permeability is independent of its humidification. Once oxygen reaches the anode catalyst layer, it reacts with hydrogen to form peroxide species, which is then decomposed in radicals in presence of metal impurities. Once created, the radicals that are highly reactive degrade the membrane, producing fluorine small chains and fluoride ions as a by-product. In the model, it is assumed that the formation of the radicals is controlled by the flux of oxygen permeating through the membrane but also by the cell voltage, as it was observed.

The cell voltage (second term) is believed to have an influence on the electrochemical formation of peroxide but also on the concentration of iron ions as suggested in the literature [23] and thus on the decomposition of peroxide into radicals. The formation of peroxide via the two-electron oxygen reduction reaction can be described using a Butler-Volmer type kinetic. Regarding the iron redox cycle, which is sustained when the cell voltage is held above 0.7 V, its detailed impact cannot be described without resorting to its comprehensive description [23]. For the sake of simplicity, it was assumed that the combination of both phenomena (peroxide formation and iron redox cycle) can be described using a Butler-Volmer type expression and using an equivalent transfer coefficient, α_{eq} .

Finally, the third term of the model expresses the fact that all the reactions leading to the chemical degradation of the membrane are temperature dependant and can be assumed to follow an Arrhenius law. The activation energy Ea stands for the equivalent activation energy of all the different reactions. It was measured by LaConti et al. and its value was found to be about 75 kJ/mol.

In the model, the impact of humidity on FRR is taken into account only through the dependence of the oxygen partial pressure to the cell humidity, since no other dependence was observed in the given experimental results.

Three experimental tests from Puma Mind project had been realized on 25 cm² single cell. Pure hydrogen was injected at anode with stoichiometry 1.2 and oxygen at cathode with stoichiometry 2. The temperature was 95°C for all the cases. Three operating conditions were defined to study the impact of low and high humidity, as well as the impact of cathode pressure on membrane degradation.

Table 4: operating condition of the Puma Mind tests for membrane degradation

PumaMind tests	Relative Humidity (%) cathode and anode	Cathode pressure (bar)	Anode pressure (bar)	Density current profile (A/cm ²) (duration (h))
Case 1	30	1.5	1.5	0.75A/cm ² (200h) - 0.4 (170) - 0.2 (205) - 0 (325)
Case 2	30	2.3	2.5	0.75 (180) - 0.4 (200) - 0.2 (195) - 0 (225)
Case 3	75	2.3	2.5	0.75 (175) - 0.2 (115) - 0.06 (150) - 0 (160)

As a first result, the sensitivity of the model to the potential has been studied for varying density current.

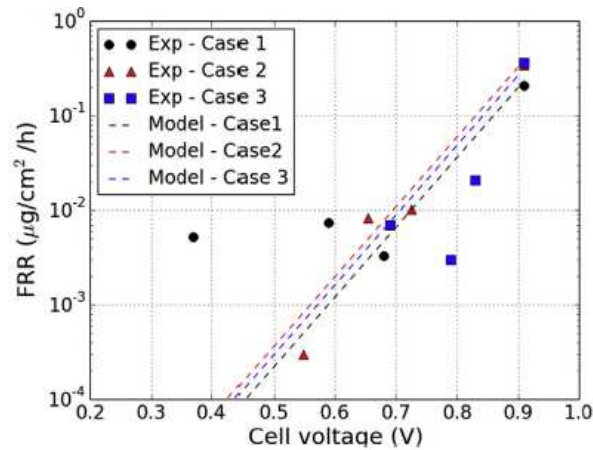


Figure 23: Influence of the potential on the FRR: comparison experiment-model (Chandesris [3])

The proposed semi-empirical model is able to capture the main observed tendency regarding the potential dependence of the FRR.

A simple model of the membrane thinning has been developed using the FRR semi-empirical model. The ionomer degradation contributes to the dry weight reduction and manifests in the membrane thinning. The evolution of the membrane thickness is supposed to be proportional to the rate of ionomer degradation. The ionomer degradation rate is related to the FRR, v_{F^-} , through the polymer chain structure. Since the FRR is normalized by the geometric active surface area of the MEA, the evolution of the membrane thickness can be assumed proportional to the FRR times the volume of dry Nafion corresponding to 1 g of Fluor:

$$\frac{de_M}{dt} = A_2 v_{F^-} v_{Nafion} \quad (32)$$

Where:

- $A_2 = 20.8$ is an empirical constant which takes into account the fact that not all the degraded ionomer fragments are recovered in the exhaust water and that the ionomer fragments are not completely decomposed into fluoride ions which are the only measured ions.
- v_F (mg/h/cm²) is the FRR given by the semi-empirical model
- V_{Nafion} is the volume of Nafion corresponding to 1g of fluorine: $V_{Nafion} = 1/(\omega \rho_N)$
- $\omega = 0.82$ is the mass fraction of fluorine in Nafion
- $\rho_N = 1980$ (kg/m³) is the density of dry Nafion.

On the figure below, the thinning of the membrane obtained from the 2 equation modelled has been compared successfully with the experiment. The cell potential decreases thanks to the membrane thinning that improves the hydrogen crossover.

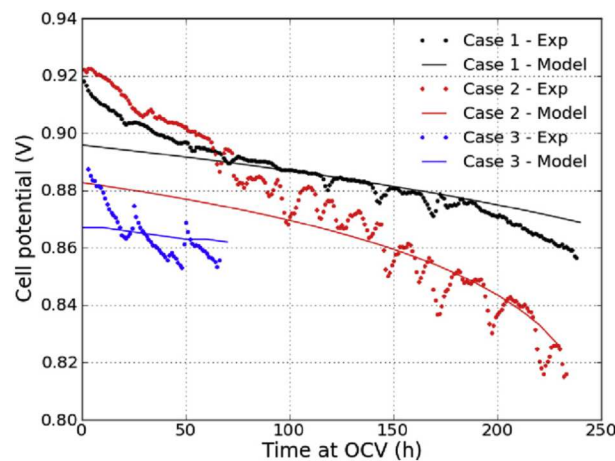


Figure 24: Simulated OCV drop induced by the membrane thinning. Comparison against experimental results. (Chandesris)

Fenton derived model

The Fenton model calculates fluoride emission through concentration of species such as H₂O₂, and the involved radicals. In its core, the description of the involved electrochemical reaction system is based on works performed at CEA dedicated to the electrolyser membrane degradation [2]. The membrane were made of Nafion 115 without catalyst layer. The main difference with fuel cell application is the thickness but the degradation process is the same.

In this work, a set of 14 electrochemical reactions was modelled as one reaction system. At first, the 14 equations model has been implemented in a standalone 0D Matlab/Simulink code and then transferred into the 2D+1D MePHYSTO code that includes all the physics of the fuel cell including the gas flux through the membrane, requested in the degradation model. For the validation, an experimental work has been performed at Aalborg University: the membrane degradation ex-situ with sensitivity to the peroxide and iron ion concentrations. 11 tests have been carried out for a 70 hours ageing of membrane with various initial concentration of peroxide and iron ion at constant temperature. The release of fluoride has been measured at various times providing its evolution along 70 hours. One of the major interests of this ex-situ study is that we expect only

membrane degradation and thus no interaction with other degradations that happen in-situ when current is applied.

The model

The main assumptions are:

- All 14 reactions occur in the same space (CL_c). Oxygen transported to the cathode is entirely and exclusively reduced to hydrogen peroxide (reaction 1)
- Reactions 2-13 follow Arrhenius behaviour
- The total fluoride emission (reaction 14) has a macroscopic reaction but behaves like an elementary reaction (i.e. also follows Arrhenius behaviour)

The model includes 14 equations with the activation energies (essentially found in the paper of Ghelichi, 2014) and the kinetic reactions:

Table 5: List of membrane chemical degradation equations used in MePHYSTO.

Reaction	E_{act} (kJ/mol)	frequency factor A (s^{-1})	Reaction number
$O_2 + 2H^+ + 2e^- \rightarrow H_2O_2$	42.45	See equation (37)	(33.1)
$H_2O_2 \rightarrow 2HO^\circ$	200	$1.09 \cdot 10^{13}$	(33.2)
$H_2O_2 + Fe^{2+} \rightarrow Fe^{3+} + HO^\circ + HO^-$	35.4	$1.03 \cdot 10^8$	(33.3)
$H_2O_2 + Fe^{3+} \rightarrow Fe^{2+} + HOO^\circ + H^+$	126	$8.31 \cdot 10^{18}$	(33.4)
$HO^\circ + Fe^{2+} \rightarrow Fe^{3+} + HO^-$	9	$8.68 \cdot 10^9$	(33.5)
$HO^\circ + H_2O_2 \rightarrow HOO^\circ + H_2O$	14	$7.66 \cdot 10^9$	(33.6)
$HO^\circ + O_2 \rightarrow HOO^\circ + H_2O$	0	$1.2 \cdot 10^7$	(33.7)
$HOO^\circ + Fe^{3+} \rightarrow Fe^{2+} + O_2 + H^+$	33	$1.21 \cdot 10^{10}$	(33.8)
$HOO^\circ + Fe^{2+} + H^+ \rightarrow Fe^{3+} + H_2O_2$	42	$2.74 \cdot 10^{13}$	(33.9)
$HOO^\circ + H_2O_2 \rightarrow H_2O + O_2 + HO^\circ$	30	$5.41 \cdot 10^5$	(33.10)
$2HOO^\circ \rightarrow H_2O_2 + O_2$	20.6	$3.5 \cdot 10^9$	(33.11)
$2HO^\circ \rightarrow H_2O_2$	7.9	$1.31 \cdot 10^{11}$	(33.12)
$HOO^\circ + HO^\circ \rightarrow H_2O + O_2$	14.2	$2.09 \cdot 10^{12}$	(33.13)
$HO^\circ + R_f - CF_2 - COOH \rightarrow product$	6.5	$1.35 \cdot 10^7$	(33.14)

In a coarse-grained approach, the rate constants at 25°C and the activation energies for reactions 33.2 to 33.13 (except for reactions 33.7, where data for only one temperature was found) were fitted to the Arrhenius equation:

$$k = A \cdot \exp\left(-\frac{E_{act}}{R \cdot T}\right) \quad (34)$$

Where k is the rate constant, A the frequency factor in s^{-1} (also known as the pre-exponential factor), E_{act} the activation energy in J/mol, R the gas constant in J/mol/K, and T the temperature in K. The rate constant for each reaction was then implemented as a function of temperature.

The concentrations of species are calculated as follows:

$$\frac{dc_s}{dt} = \sum_{rxn=i} (v_{s,i} \cdot r_i) + V_{s,in} - V_{s,out} \quad (35)$$

Where v_s is the stoichiometric factor of species s in reaction i , r_i the reaction rate of reaction (33.i) in $mol/m^3/s$, and $V_{s,in}$ and $V_{s,out}$ the volumetric flow rate of species s in and out of the modelled volume in $mol/m^3/s$, respectively. The stoichiometric factor is negative for reactants and positive for products by convention. It is furthermore assumed to be zero if the species does not participate in the reaction. The molar fluxes are calculated by MePHYSTO. All the concentration must be initialized to solve the equations. In case of in-situ simulation, all the species have zero initial concentration. For the ex-situ simulation, the initial values for $[Fe^{2+}]$ and $[H_2O_2]$ have been set to their experimental values and the other ones to zero.

The hydrogen peroxide is the precursor of the considered reaction system (reaction 33.1), necessary for the membrane attack. The source of H_2O_2 is the oxygen that crossed the membrane and reduced on the Pt catalyst. The reaction kinetic is modelled by the following equations:

$$r_1 = k_1 \cdot c_{O_2} \cdot c_{H^+}^2 \quad (36)$$

Where c_{O_2} and c_{H^+} are the oxygen and proton concentrations, respectively, and the rate constant k_1 is given by:

$$k_1 = k_1^0 \cdot \exp\left(\frac{-E_{act,1}}{R \cdot T}\right) \cdot \exp\left(\frac{-\alpha_{H_2O_2} \cdot F \cdot \eta_{H_2O_2}}{R \cdot T^0}\right) \quad (37)$$

where R , F , and T have their generic meaning, $E_{act,1}$ is the activation energy for reaction (33.1), and $\alpha_{H_2O_2}$ and $\eta_{H_2O_2}$ are the transfer coefficient and equilibrium potential, respectively.

$$k_1^0 = 706.8 \cdot 10^{-14} m^7 \cdot mol^{-2} \cdot s^{-1}$$

While the oxygen concentration is dictated by the dynamics of the reaction system, the proton concentration is dependent on the ionomer humidification and implemented as follows:

$$c_{H^+} = \frac{\rho_{PFSA}(\lambda)}{EW} \quad (38)$$

Where $\rho_{PFSA}(\lambda)$ and EW are the humidity-dependent density and the equivalent weight of the ionomer, respectively.

In this work it is proposed that the radicals formed as described by reactions (33.2) to (33.13) attack the ionomer structure at their weak carboxylic acid end-groups (-COOH) (Shah, 2009). The

attack reaction (33.14) is of second order and affected by the concentrations of hydroxyl radicals (HO^\bullet) and reactive end-groups of the polymer ($-\text{COOH}$). While the HO^\bullet concentration is calculated within the reaction system, the concentration of $-\text{COOH}$ end-groups is subject of discussion. In this work, a constant value of 200mM is chosen. This lies within the values found in the literature, where a constant concentration of 1.17M, representing 5% of the total CF_2 count in the polymer main chain, can be found [9]. We interpret this value as an upper limit, while bringing to the attention that a value of around 2mM to 20mM would have to be assumed according to Zhou [25]. A sensitivity analysis of the parameter is carried out below as shown in Figure 25. The reaction rate constant k_{14} was not found for any other temperature than room temperature in the literature. Therefore, the gathered data at 80°C together with the reported value at 25°C are utilized to fit an Arrhenius law for k_{14} .

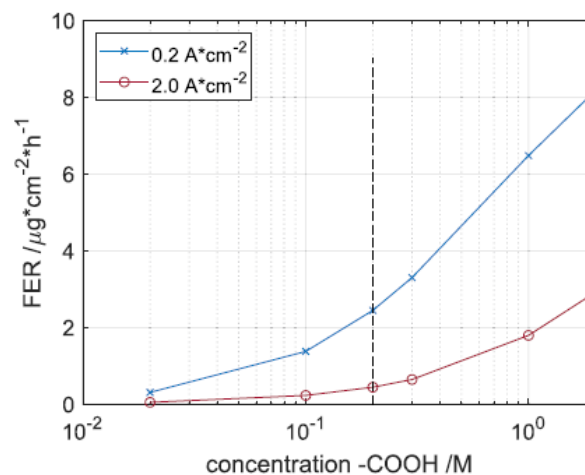


Figure 25: Impact of the concentration of reactive eCOOH end-groups on Fe^{2+} concentration (blue) and FER (red). The value used for this work of 200mM is marked with the dashed line.

To quantify membrane thinning through fluoride emission, a relationship between fluoride content and membrane volume has to be established. We use the equation (32) already given previously in the semi-empirical model.

Experiment

Eleven polypropylene flasks were filled with 100mL ultra-pure water for the ex-situ experiment. A specific initial concentration of Fe^{2+} and H_2O_2 according to the following table, was established based on a literature review of previous tests. The iron concentration was set through iron (II) sulfate heptahydrate ($\text{FeSO}_4\cdot 7\text{H}_2\text{O}$, Merck KGaA) and the hydrogen peroxide concentration through 33% H_2O_2 solution (VWR Chemicals). 25 cm² Nafion® 115 cut into five pieces was immersed and each experiment lasted for 72 h at 80 °C inside an oven. The fluoride content was monitored frequently with an ion selective electrode (ISE, Hach Company ISE301F combined electrode).

Table 6: Experimental matrix for the ex-situ Fenton test. All concentrations refer to their initial value. The highlighted condition is the baseline test

EXP	[Fe ²⁺] / ppm	[H ₂ O ₂] / wt%
#1	0	0
#2	1	0
#3	1	0.003
#4	1	0.03
#5	1	0.3
#6	1	3
#7	1	30
#8	0	3
#9	0.1	3
#10	10	3
#11	20	3

Experimental results

The fluoride concentrations of the 11 tests are plotted against time on the following figure. Experiments with varying initial concentration [H₂O₂] are shown in solid lines and varying initial [Fe²⁺] concentrations in dashed lines together with the baseline and the pure water test in dash-dot lines. Some conclusions can be drawn:

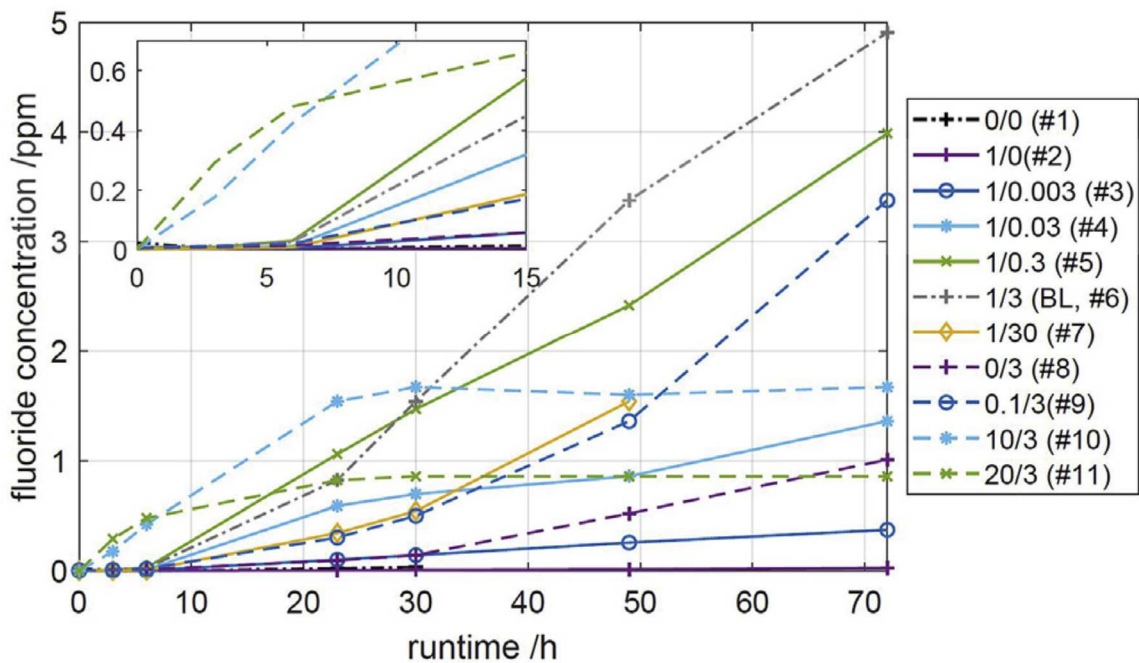
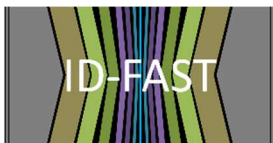


Figure 26: Fluoride concentration over time for all experiments. The legend refers to the initial concentrations as [Fe²⁺]/[H₂O₂], where BL=baseline test.



As expected, the test with neither H_2O_2 nor Fe^{2+} initially (#1) only shows a negligible fluoride release. The experiment with no H_2O_2 and 1ppm Fe^{2+} (#2) also exhibits almost no fluoride emission, while the presence of 3wt% H_2O_2 but no Fe^{2+} (#8) lead to a considerable fluoride concentration especially towards the end of the experiment of around 1ppm. This observation supports the above presented assumption that H_2O_2 is as an obligatory precursor for the whole reaction system, while Fe^{2+} acts as a catalyst.

Before analysing the effect of the initial species concentration in more detail, two different trends can be observed for the reaction kinetics of fluoride emission: Firstly, a steep increase in the first hours, followed by a constant concentration after around 23h, and secondly, a rate that starts slowly and accelerates over time. The two experiments with high initial Fe^{2+} concentration (#10 and #11) follow the first trend, while all others tend to follow the second. The second category may exhibit an exponential behaviour, where experiments with very low initial H_2O_2 concentration (#1, #2, and #3) arguably follow a more linear trend in the investigated time-frame. A longer period of time would have to be investigated in order to observe an asymptotic behaviour. For all tests except the ones with high initial Fe^{2+} concentration, the fluoride concentration is below or just around the detection limit of $5 \cdot 10^{-7}\text{M}$ ($= 0.0095\text{ppm}$) within the first 3 to 6 hours of test as shown in the magnification in Figure 26.

The flattening of the curves with high initial Fe^{2+} concentration is connected to H_2O_2 exhaustion. With Fe^{2+} as a strong catalyst, the initial H_2O_2 may be used up fast with nothing left to run the reaction over a longer time. Therefore, H_2O_2 represent the limiting reactant in these experiments. Consequently, the final fluoride concentration after the test was terminated may be significantly higher if more H_2O_2 was available, either as an initial concentration or as a steady influx. It can in fact be observed, that the highest initial Fe^{2+} concentration of 20ppm led to highest fluoride emission measured after 3h as shown in the magnification in Figure 26. Possibly due to the same limiting effect, 10ppm Fe^{2+} (#10) produced less fluoride emission than 1ppm Fe^{2+} (#6) after the initial H_2O_2 is completely used up. This appears to be the case after around 30h. Therefore, a peak appears at 10ppm after 23h when plotting the fluoride concentration over initial Fe^{2+} concentration as seen in Figure 27a. This peak shifts to 1ppm after 49h, when H_2O_2 became limiting for the test at 10ppm. Therefore, it is expected that a higher Fe^{2+} concentration leads to a higher fluoride emission as long as sufficient H_2O_2 is present.

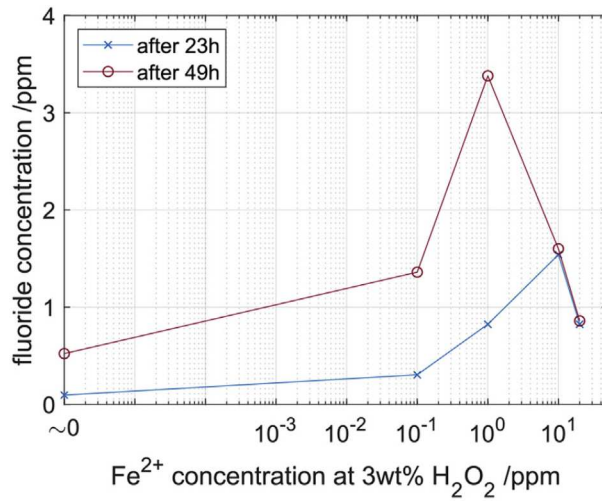
When looking at the experiment without any initial Fe^{2+} (#8), an unexpectedly high fluoride emission can be observed. Although Fe^{2+} only acts as a catalyst and is theoretically not necessary to produce HO° radicals as shown in reaction 33.2. This discrepancy might be explained by the presence of other metal impurities such as copper ions (Cu^{2+}) in the solution, which catalyse the Fenton reaction but are not implemented in the model. They may stem for example from the membrane manufacturing process or the feed water that may not be purified perfectly. Furthermore, it has been shown in the literature that Fe^{2+} may be replaced by other Fenton-like metal catalysts to produce HO° radicals, including titanium.



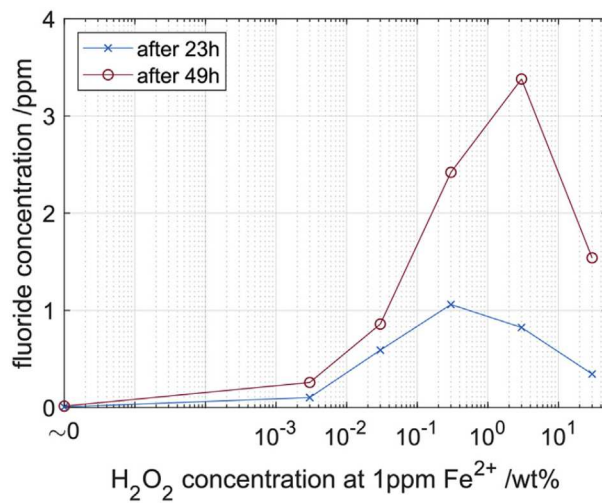
D3.1: Report on models describing the main degradations modes and analysis of their stressing factors



The impact of initial H_2O_2 concentration on fluoride emission at 1ppm initial Fe^{2+} concentration can be seen in Figure 27b. As for iron, the figure includes measurements after 23h (blue) and 49h (red). Besides the above mentioned zero-emission at the absence of H_2O_2 , a dependency is visible. While low initial H_2O_2 concentration leads to low fluoride emission, the peak is reached between 0.03 and 30wt%, depending on the considered time-frame. This suggests the existence of an optimal concentration to prevent excessive membrane degradation outside these boundaries. In short, the reason is that reaction (33.6) becomes dominant over the membrane attack reaction (33.14) at high H_2O_2 concentrations, effectively depleting HO° radicals without fluoride emission. However, intuitively an increase in fluoride emission with H_2O_2 concentration would be expected. A repetition of the set of experiments has to be carried out in order to finally conclude on the existence of an optimum and to rule out experimental errors.



(a) Measured fluoride concentration as a function of initial Fe²⁺ concentration



(b) Measured fluoride concentration as a function of initial H₂O₂ concentration

Figure 27: Influence of initial Fe²⁺ and H₂O₂ concentration.

Simulation of the Membrane Attack Reaction

The model described above (equations 33.i) is utilized in order to simulate ex-situ behaviour and adjusted by setting all in and outflux to zero. Instead, the initial concentrations of Fe²⁺ and H₂O₂ are set according to the test as in Table 6. Furthermore, the initial oxygen concentration was set according to Henry's law due to dilution from the air.

The simulations of tests with no iron nor peroxide (#1, #2 and #8) lead to zero emission since the model request both (the curves are not shown to lighten the figures). In in-situ test, peroxide would be present but most of the time we ignore the presence of iron ions which concentration have to be estimated. A model for bipolar plate corrosion would be an interesting starting point to evaluate it. All the simulations have been performed until the FRR has reached its asymptotic value. The time scale to reach this value depends on the initial Fe^{2+} and H_2O_2 concentrations as illustrated on the Table 7.

The simulations shows that the iron ions Fe^{2+} convert nearly instantaneously into Fe^{3+} as illustrated on the Figure 28.

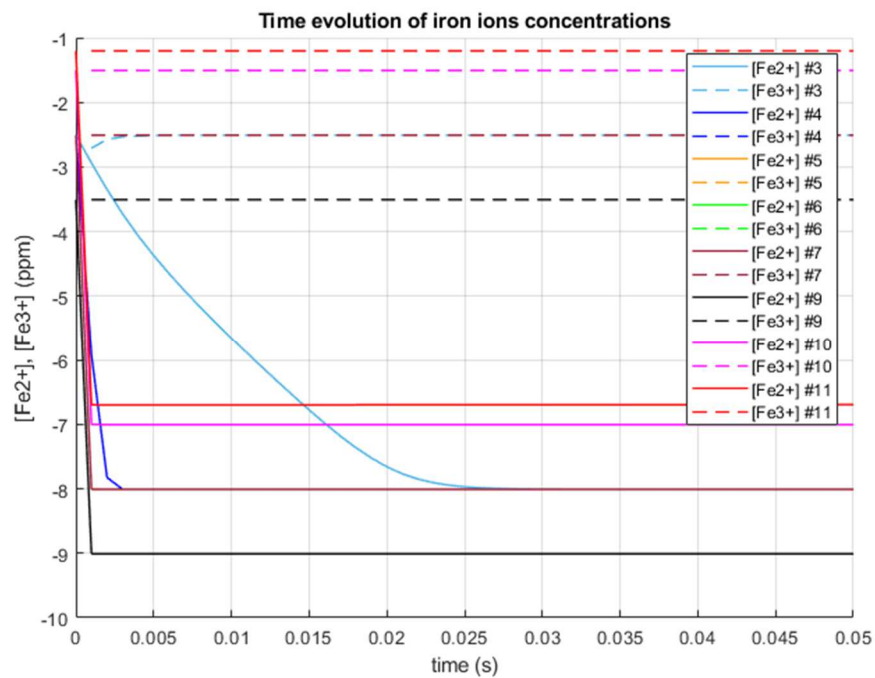


Figure 28: Simulated iron ion concentrations ($\log_{10}([\text{Fe}^{2+}])$, $\log_{10}([\text{Fe}^{3+}])$).

The comparison of experimental and simulated Fluoride concentrations evolving against time is plotted on the Figure 29 for the tests 3, 4, 5, 6, 7, 9, 10 and 11. The tests 1, 2 and 8 are not plotted since without initial peroxide or iron, the model does not predict fluoride release. For each test we have plotted four graphs for temporal evolutions of the following quantities:

- on the top and left graph, the velocities of all the 14 equations,
- on the bottom left, the velocities of the main quantities involved in the Fenton process,
- on the top right, the concentrations of these quantities,
- on the bottom right the comparison between measured and simulated Fluoride concentrations. A summary of these results is plotted on the Figure 30 for the final time (72h) of the experiment.

The membrane thickness evolution is plotted on the Figure 31 for all the relevant tests.



Several comments have to be drawn:

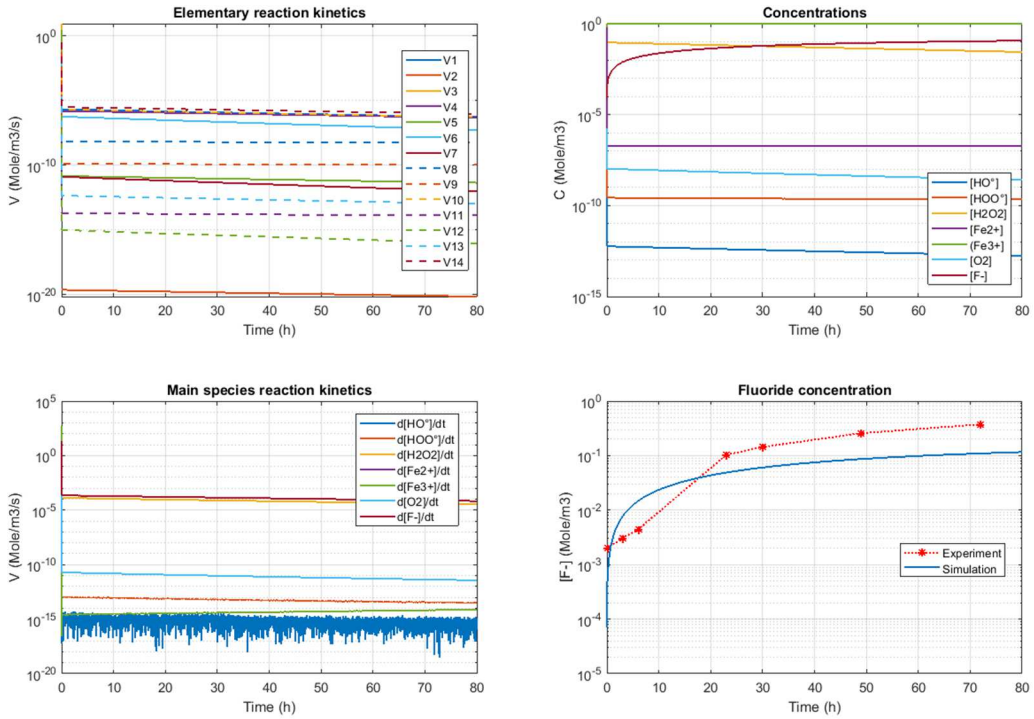
- Most of the experiments have not reached their asymptotes at 72h, the final time, and thus, it is not possible to conclude definitively on the final agreement between experimental data and simulations except for the tests 10 and 11 corresponding to very high initial hydrogen peroxide and iron ions concentrations.
- For the known part of the experimental results, the model predicts correct tendencies and orders of magnitude for the Fluoride concentrations even if the time scale seems too small (the simulated concentrations reach their asymptotes too rapidly). This last point could be not really a problem for long term degradations.
- For the tests 10 and 11, the simulated Fluoride concentration is overestimated by a ratio equal to 2.7 and 4.9 respectively. This difference might come from the various uncertainties on the model parameters (activation energy, frequency factor, concentration of the polymer end group ...). It could also result from a saturation mechanism that is not modelled or from a different reaction order induced by these very high initial concentration of hydrogen peroxide. These very high concentrations will be compared later to in-situ simulations ones in order to determine if they are realistic or not and therefore if the model for these situations has to be improved or not.
- From the *main species reaction kinetics* graphs, it is clear that the Fluoride concentration dynamic follow the hydrogen peroxide concentration one. Looking at the *concentrations* graphs, only iron ions (Fe^{3+}), hydrogen peroxide and Fluoride concentrations have corresponding order of magnitudes. All the others are quite lower
- Not all the equations play an equivalent role as illustrated on the elementary reaction kinetics graphs. We have summarised in Table 7 the number of the reactions that are quantitatively the most important (by at least one order of magnitude) during the whole simulation. Not surprisingly the reaction (33.2) is negligible due to its slow kinetic. Reactions (33.5), (33.7), (33.9), (33.11), (33.12) and (33.13) seems to be negligible in these conditions. Thus only 7 equations really play a significant role in our simulations. This point should be checked using in-situ experiments. The reduction of the number of reaction and thus of equations to be solved can help to reduce the CPU time for long term simulations.
- The membrane thickness evolution has not been measured, thus we can only conclude that the model predicts a non-negligible decrease of the thickness, to $3\mu\text{m}$ for 80h. The decreases take place essentially at the beginning of the simulations in agreement with dynamic of the Fluoride releases rates.



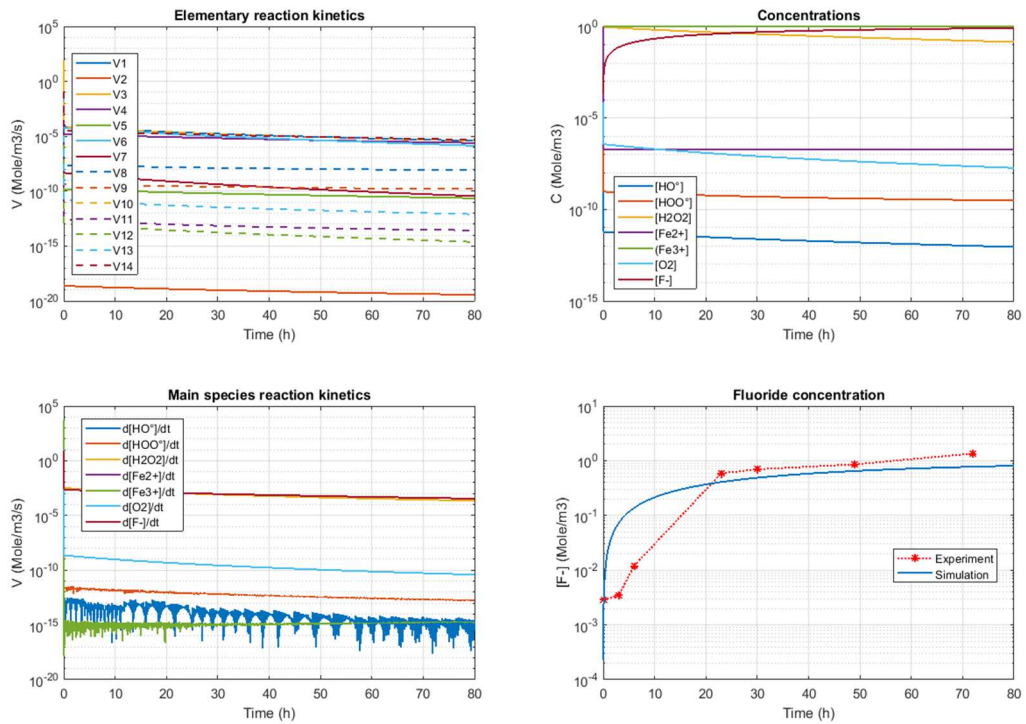
D3.1: Report on models describing the main degradations modes and analysis of their stressing factors



Test 3 : H2O2 = 30 ppm - Fe++ = 1 ppm



Test 4 : H2O2 = 300 ppm - Fe++ = 1 ppm

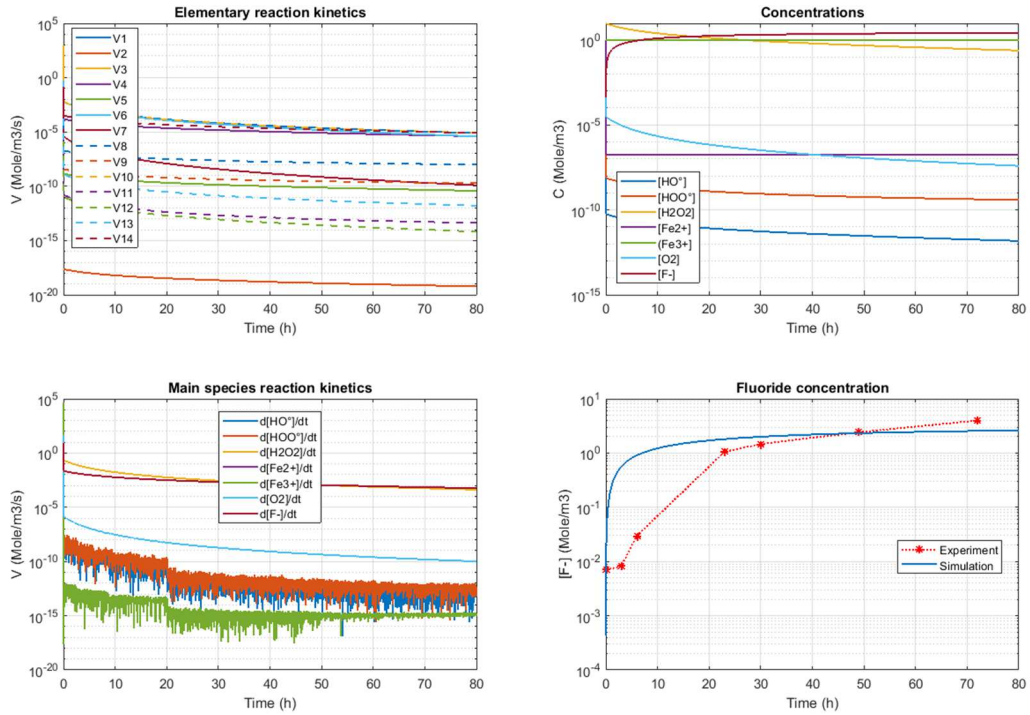




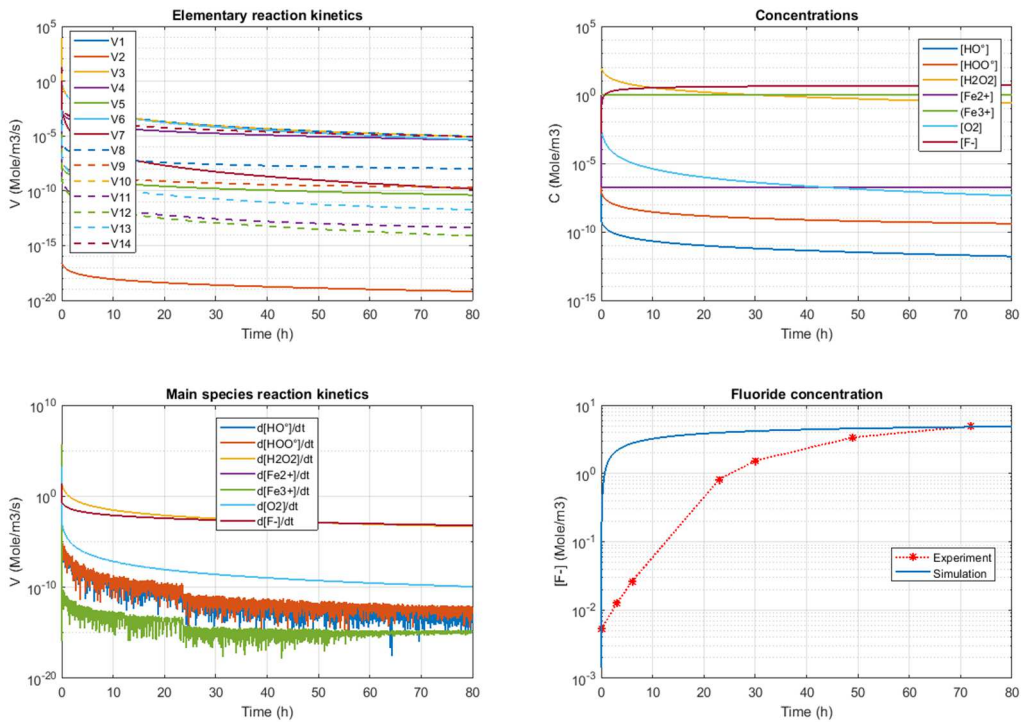
D3.1: Report on models describing the main degradations modes and analysis of their stressing factors



Test 5 : H2O2 = 3000 ppm - Fe++ = 1 ppm



Test 6 : H2O2 = 30000 ppm - Fe++ = 1 ppm

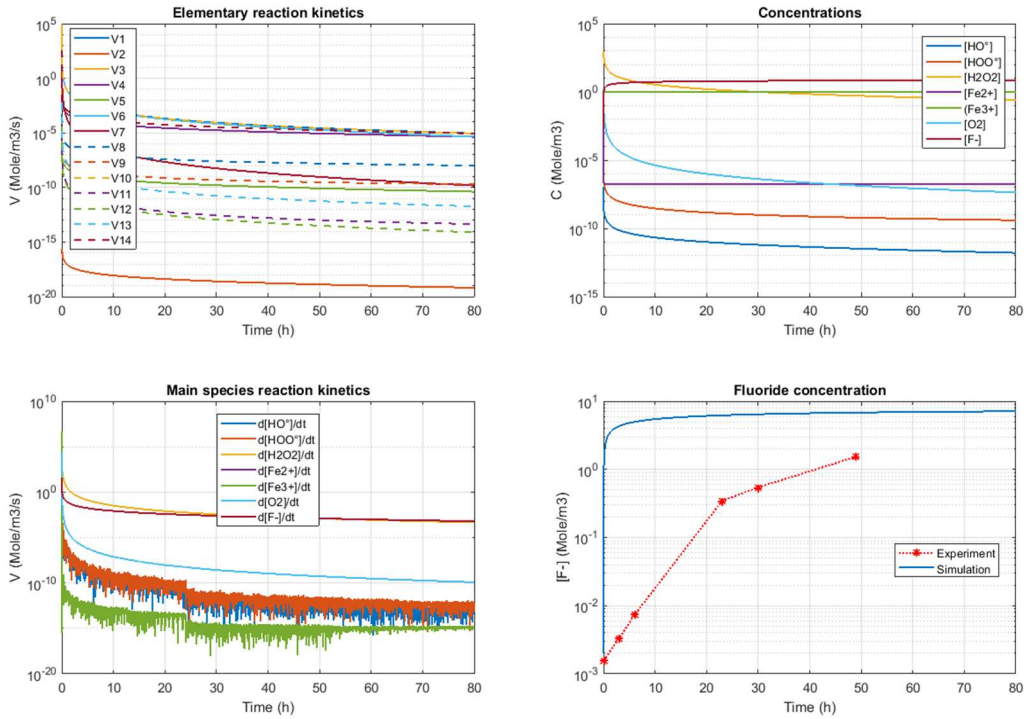




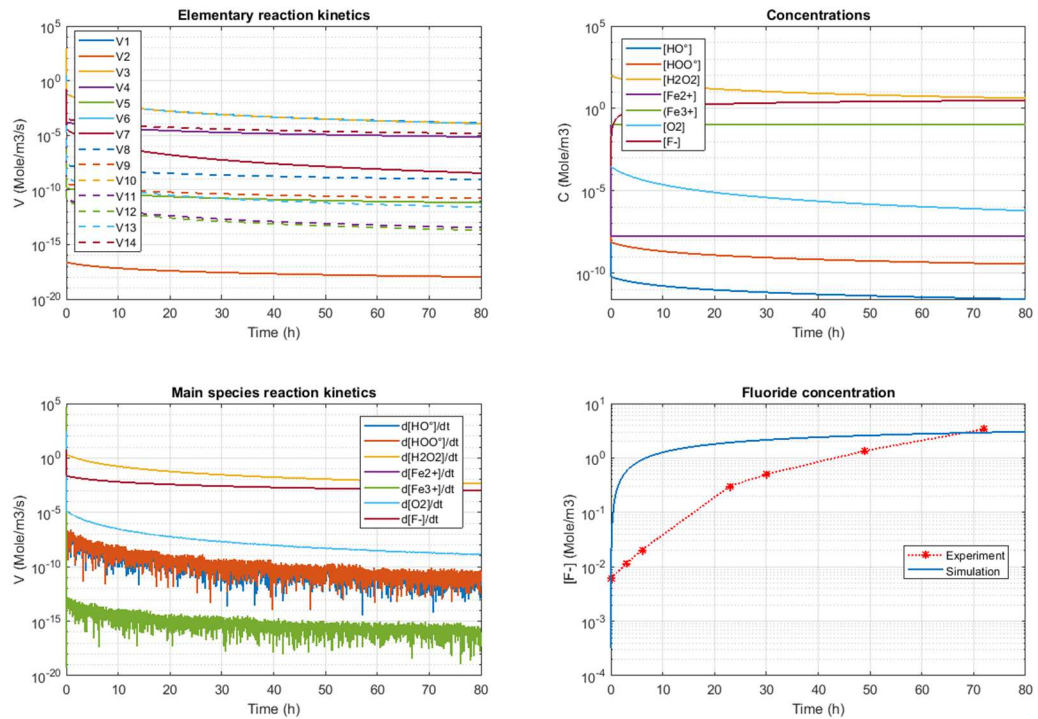
D3.1: Report on models describing the main degradations modes and analysis of their stressing factors



Test 7 : H2O2 = 300000 ppm - Fe++ = 1 ppm



Test 9 : H2O2 = 30000 ppm - Fe++ = 0.1 ppm



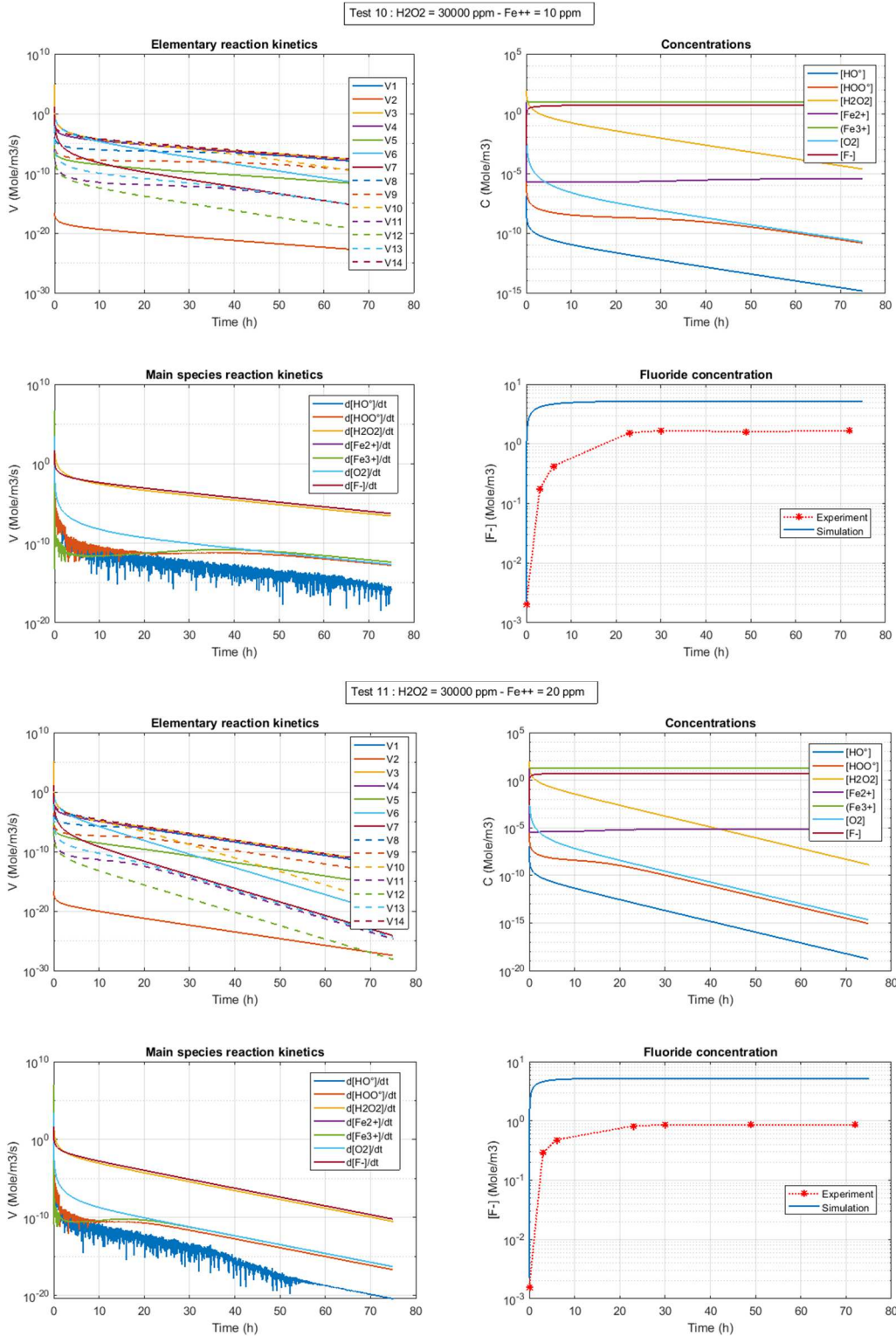


Figure 29: Velocities and concentrations of all species for tests 3, 4, 5, 6, 7, 9, 10, 11

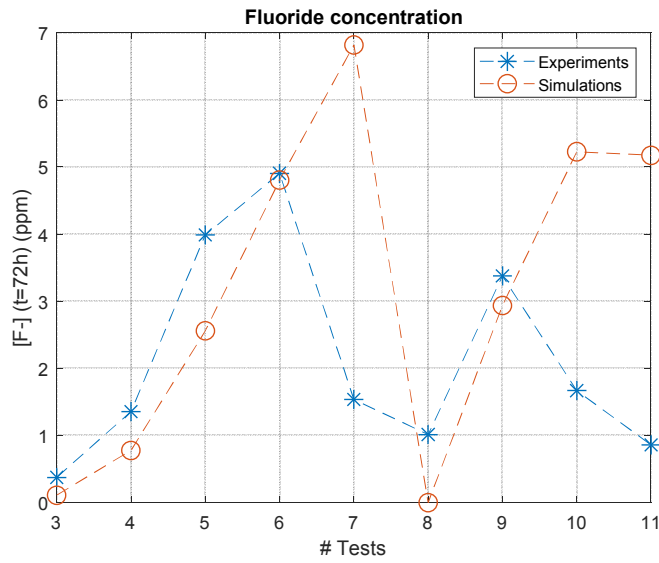


Figure 30: Measured and simulated Fluoride concentrations for tests 3, 4, 5, 6, 7, 9, 10, 11

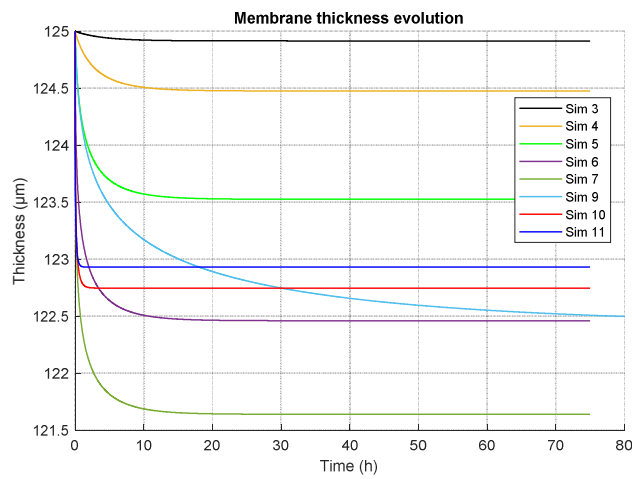


Figure 31: Simulated membrane thickness evolution for tests 3, 4, 5, 6, 7, 9, 10, 11

Table 7: Matrix for the ex-situ test: time scales and important reactions (see the reaction number in Table 5).

EXP#	[Fe ²⁺] / ppm	[H ₂ O ₂] /wt%	Time to reach asymptote (h) (experimental)	Important reactions at asymptote 33.i
#3	1	0.003	20	1 3 4 6 10 14
#4	1	0.03	20	1 3 4 6 10 14
#5	1	0.3	20	1 3 4 6 10 14
#6	1	3	20	1 3 4 6 10 14
#7	1	30	20	1 3 4 6 10 14
#9	0.1	3	150	1 3 4 6 10 14
#10	10	3	5 (30)	1 3 4 6 8 10 14
#11	20	3	5 (30)	1 3 4 6 8 10 14

As a first conclusion on this Fenton model, globally the orders of magnitude are captured, the tendencies are correct but the time scales are underestimated and some discrepancies between final measured and simulated Fluoride concentrations are noticed for very high initial hydrogen peroxide concentrations. It is possible that these particular situations (tests 12 and 11) are non-realistic and that the first order reaction is not yet a valid hypothesis. The model is based on several parameters that are known with uncertainties, thus, a sensitivity studies could be interesting when more data will be available. The analysis of the various results has shown that only half of the model equations play a significant quantitative role and the others seems negligible. This point has to be confirmed performing more simulations for other situations such as in-situ ones. Another way of analysis could be to perform these simulations using the degradation model developed at DLR [8] and to make comparisons. The model simulates a non-negligible decrease of the membrane thickness that is not validated yet due to the lack of data. More experimental data, in situ and if possible ex-situ, are requested before going further.

4.3. Conclusions on the membrane degradation models

Two models have been described: a semi-empirical one developed at CEA, fitted on experimental data, it provides good results. But, since it is fitted on a few amount data, more experimental are requested in order to extend its validity. Some recommendations are given in the original paper[3] to increase the input parameters and thus its capability to describe various situations. This way seems promising and will be explored. The 2nd model, also developed at CEA, is based on the Fenton process. It includes about 15 differential equations. The first validation is based on ex-situ experiments. The results are qualitatively correct but quantitatively perfectible especially at very high peroxide concentrations. More experimental data are requested in order to fit the chemical parameters of this model and to try to add equations that take into account the complexity of the Nafion degradation [8].

5. GDL degradation model

5.1. Scientific approach and model description

Aim of this work is to understand and model the gas diffusion layer (GDL) degradation due to loss of hydrophobic binder (PTFE). Integration of this model into single cell CFD models shall allow for simulation of the impact of PTFE loss on the local effective transport parameters and therefore the cell performance.

The workflow of our approach in building up the cell level PTFE degradation model comprises of three major steps, as they are depicted in Figure 32.

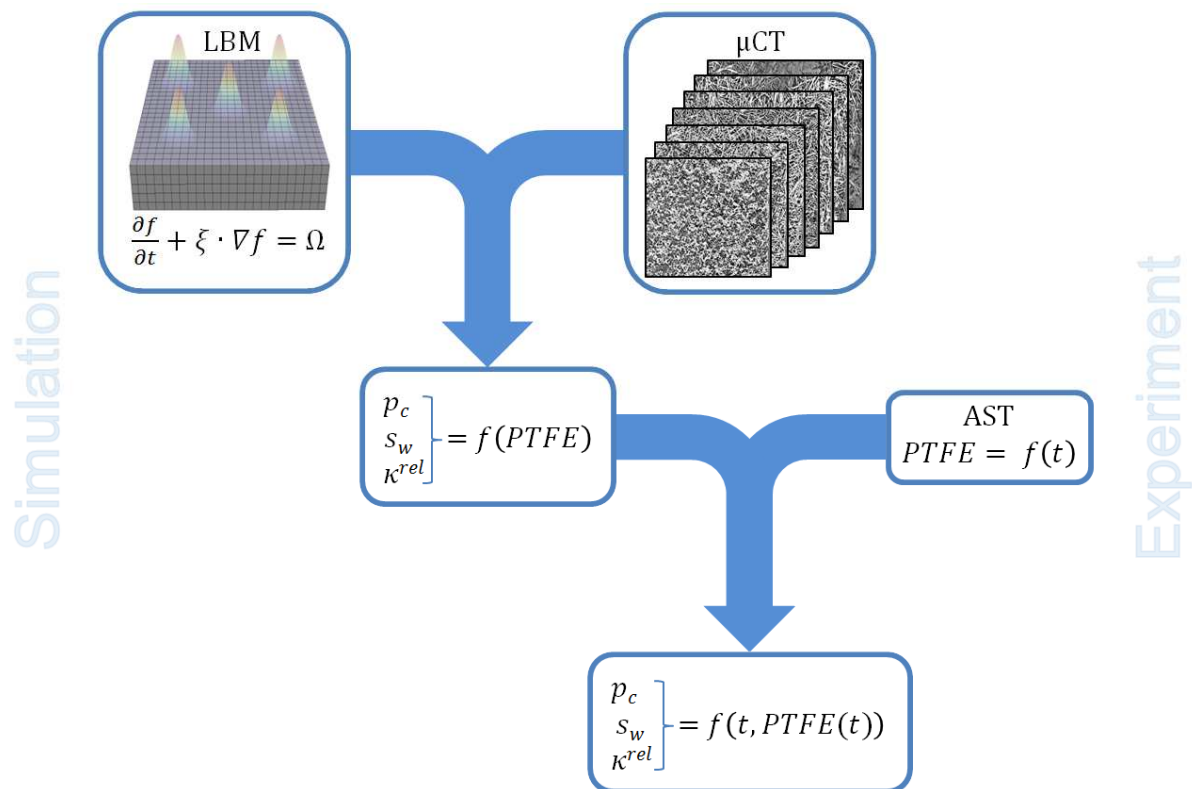


Figure 32: Conceptual workflow for the derivation of a PTFE degradation model within the gas diffusion layers of PEMFCs.

In a first step we investigate the general influence of PTFE content on effective transport parameters within the GDL. For this we investigate liquid water transport through the porous microstructures by conducting mesoscopic simulations using the Lattice Boltzmann method on reconstructed μ CT images. The outcome of these studies is an interconnected dependency of capillary pressure, saturation and relative permeabilities on the PTFE content within the GDL.



Subsequently we build up a second model for the degradation rate of PTFE over time. For this, we evaluate accelerated stress tests (ASTs) to identify the amount of PTFE that is lost on cell level over operation time depending on the applied stressors.

In a third and final step, we couple the findings from mesoscale simulations and cell-level degradation tests. We combine the PTFE-dependence of effective transport parameters from LBM simulations and the temporal degradation rate of PTFE. In doing so, we arrive at an interdependence of capillary pressure, saturation and relative permeabilities on PTFE content and time. Incorporating these dependencies into a transient single cell model will then allow simulations of the effect of PTFE degradation on cell performance.

5.2. Lattice-Boltzmann modelling of effective transport parameters in porous gas diffusion media

5.2.1. Model description

Liquid water transport within the microstructures of the GDL is modelled using the mesoscopic Lattice Boltzmann method (LBM). Therein the Boltzmann equation is discretized and solved over a simulation domain in form of a lattice with m lattice dimensions and n lattice directions (DmQn model).

$$f_i(x + e_i \Delta t, t + \Delta t) = f_i(x, t) + \Omega(f_i(x, t)) \quad (39)$$

The Boltzmann equation describes the state of a system by the temporal evolution of a velocity distribution function $f_i(x, t)$. This fundamental quantity is a probability density for particle presence in a given state x in 2^*m dimensional phase space and the subscript i denotes the respective lattice direction. Ω appears as a general source term on the evolution of f_i and is in the case of single-phase flow equivalent to a single phase collision operator. For the sake of simplicity the choice is often restricted to a single-relaxation time (SRT) operator, of which the Bhatnagar-Gross-Krook[1] (BGK) is the most popular one:

$$\Omega^{\text{BGK}}(f_i(x, t)) = \omega_{eff} [f_i(x, t) - f_i^{eq}(x, t)] \quad (40)$$

In this formulation ω_{eff} is a relaxation parameter determining the speed of approaching local equilibrium. With the BGK operator the evolution of f_i is then given as follows:

$$f_i^{\text{single-phase}}(x + e_i \Delta t, t + \Delta t) = f_i(x, t) + \omega_{eff} [f_i(x, t) - f_i^{eq}(x, t)] \quad (41)$$

Temporal change in the velocity distribution is therefore linearly dependent on the equilibrium distribution f_i^{eq} , which can be derived from kinetic theory[19]. It is a function of the fluid's density ρ and velocity u , as well as a lattice-specific compressibility ϕ_i , weight W_i and lattice velocity c_i for each lattice direction.

$$f_i^{eq}(x, t) = \rho \left(\phi_i + W_i \left[3c_i \cdot u + \frac{9}{2}(c_i \cdot u)^2 - \frac{3}{2}u \cdot u \right] \right) \quad (42)$$



Simulation of multiple phases requires an extension of the single-phase LBM model, for this several popular concepts exist. One of these models originates from a work by Rothman & Keller[18], where a system of two phases is considered as a 'red' and a 'blue' fluid.

$$f_i(x, t) = f_i^r(x, t) + f_i^b(x, t) \quad (43)$$

In this color-gradient model (CGM) surface tension is created by employing a perturbation operator[16] after the single-phase collision.

$$f_i^{\text{pert}} = f_i^{\text{single-phase}} + \Delta f_i^{\text{pert}} \quad (44)$$

$$\Delta f_i^{\text{pert}} = A|\Phi| \left[W_i \frac{(\Phi \cdot c_i)^2}{|\Phi|} - B_i \right] \quad (45)$$

Alteration of the single-phase distributions through the perturbation step depends majorly on a color-gradient Φ , which approximates the interface normal between the two fluids and is commonly calculated using isotropic discretization schemes[13].

$$\Phi = \nabla \left(\frac{\rho_r - \rho_b}{\rho_r + \rho_b} \right) \quad (46)$$

Desired surface tension σ is then imposed on the system by adjusting the value of parameter A accordingly[14, 16]. Furthermore the parameter set B_i is lattice-dependent and has to be chosen such that mass conservation is maintained.

$$A = \frac{9}{4} \omega_{eff} \sigma \quad (47)$$

The perturbation operator generates surface tension, but it does not guarantee immiscibility of the two phases, therefore a recoloring operator[20] needs to be employed in succession to the perturbation step.

$$f_i^{r, \text{recol}} = \frac{\rho_r}{\rho} f_i^{\text{pert}} + \beta \frac{\rho_r \rho_b}{\rho^2} \cos(\nu_i) f_i^{eq}(x_{u=0}, t) \quad (48)$$

$$f_i^{b, \text{recol}} = \frac{\rho_b}{\rho} f_i^{\text{pert}} - \beta \frac{\rho_r \rho_b}{\rho^2} \cos(\nu_i) f_i^{eq}(x_{u=0}, t) \quad (49)$$

Distributions are therefore relocated perpendicular to the interface with ν_i as the angle between lattice direction and color-gradient and $f_i^{eq}(x_{u=0}, t)$ as the equilibrium distribution of the interface, assuming a net velocity of zero for the fluid.

Lastly new distributions of a lattice node have to be streamed out for each phase and have to be reassigned to the next neighboring sites along the lattice.

$$f_i^k(x + e_i \Delta t, t + \Delta t) = f_i^{k, \text{recol}}(x, t) \quad (50)$$



5.2.2. Boundary conditions

In the two-phase Lattice-Boltzmann methodology, fluid-fluid interactions are fully defined by the perturbation operator in equation (45) and by setting a value for the surface tension (eq. (47)). If one wants to consider solid phases as well, further boundary conditions have to be specified for the interactions between solid-fluid and solid-fluid-fluid (three-phase interface) nodes. In the first case solid boundaries are modeled with a no-slip condition using the full-way bounce back scheme[5]. In the latter case of a three-phase interface between a solid boundary and two fluids, a contact angle is defined for the respective material (e.g. carbon or PTFE) in the solid phase. For this, fictitious densities are set on solid boundary nodes, following the standard wetting boundary approach[12].

$$\rho_s^{liq} = \rho + 0.5\rho \cos(\theta_c) \quad (51)$$

$$\rho_s^{gas} = \rho + 0.5\rho \cos(180 - \theta_c) \quad (52)$$

With a look on equations ((51)) and ((52)) it is clear, that $\theta_c < 90^\circ$ results in a favored transport of the liquid phase (wetting phase) along the solid boundary. A value of $\theta_c > 90^\circ$ leads to a hampered movement of the liquid phase near solid nodes, it is now regarded as non-wetting, owing to the hydrophobicity of the solid material.

Transport of phases through the system can also be promoted or impeded by the use of domain boundary conditions, which are (at least in LB-type simulations) most commonly defined as pressure or velocity boundary conditions. In this work system pressure is controlled by imposing single phase densities at in- and outlet boundaries of the simulation domain with the formulation of Zou & He[26]. The remaining, unspecified domain boundaries are treated with periodic boundary conditions.

5.2.3. Microstructure reconstruction of μ CT images

One of the advantages of the Lattice Boltzmann methodology is, that simulations can be easily carried out on geometries with arbitrary shape and arbitrary physical resolution. Therefore it is convenient to use real geometrical data for the setup of the simulation domain. In this work we used information from μ CT imaging technique to resolve real GDL microstructures to be used as binarized structural data in our LBM simulations.

The images had a resolution of $0.96 \mu\text{m}$ per pixel and were preprocessed within Geodict[27] using a sharpening and a median filter, each with 1 voxel radius. The binarization procedure of choosing a grey threshold value was done by manual thresholding. For this a sensitivity study was conducted to analyze the influence of the threshold value on the porosity and the pore size distribution (PSD), of which both were determined using Geodict. They were compared with manufacturer specifications and an in-house porosimetry measurement respectively. After the thresholding a second sensitivity study was undertaken to investigate the influence of the domain size on the PSD, the results were again compared to an in-house porosimetry measurement (Figure 33).

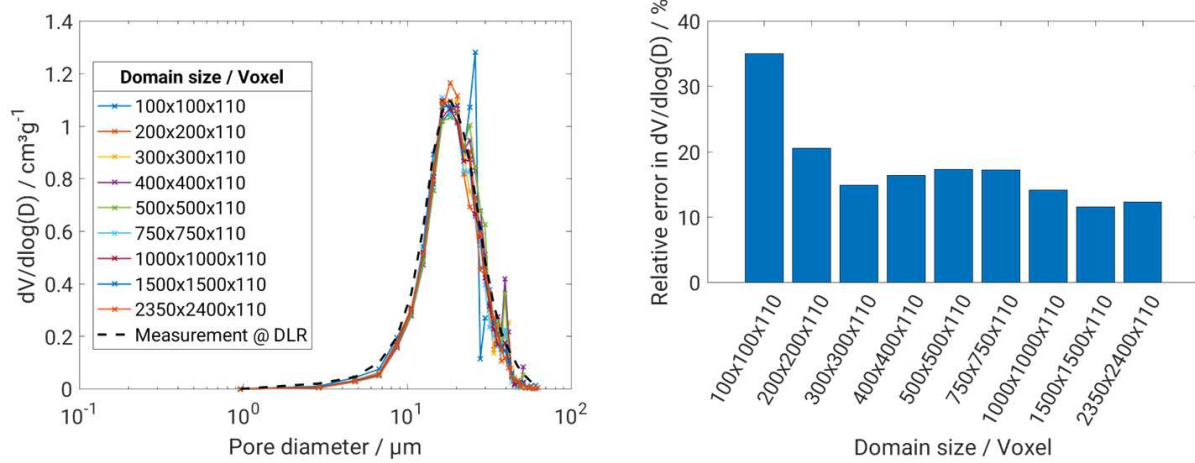


Figure 33: Left: PSDs from simulations in Geodict for different domain sizes compared to an in-house porosimetry measurement. Right: Relative errors of simulated PSDs in reference to in-house measurement.

Polymeric compound such as PTFE can be hardly detected and distinguished using the CT imaging technique, therefore it was yet only possible to resolve support material in form of carbon fibers. To be able to include PTFE into the simulation domains nevertheless, the Geodict module *AddBinder* was utilized to distribute binder material homogeneously over the binarized carbon support microstructure up to a desired weight content of PTFE.

Similarly also the MPL structure cannot be fully resolved by μCT scanning, for which reason only the macro-pores of the MPL were analyzed and binarized, assuming that they are predominantly affecting liquid phase transport through the GDL.

5.2.4. Numerical setup

Beforehand described two-phase Lattice-Boltzmann model was employed on a three-dimensional lattice using a velocity set of 19 different directions (D3Q19 model). The grid of the binarized GDL microstructure encompassed 200x200x110 voxels with a physical spacing of $0.96\mu\text{m}$ per voxel. On one side of this domain (CL side), a liquid phase inlet boundary layer was added, containing the binarized macro-pores of one MPL layer. On the other side, i.e., the channel side, a void boundary layer for the gas phase was appended.

System pressure was controlled by setting phase pressures at the boundary layers using the boundary condition by Zou & He[26]. Whilst on the gas channel side gas phase pressure was kept at unity, variable liquid phase pressures were set for the pore space of the macro-pores within the MPL boundary layer. Using this boundary setup, a capillary pressure ($\Delta p^{cap} = p^{liq} - p^{gas}$) was induced on the system, perpendicular to the through-plane direction of the GDL microstructure. For the boundaries in the in-plane direction periodicity was assumed and therefore periodic boundary conditions were employed.

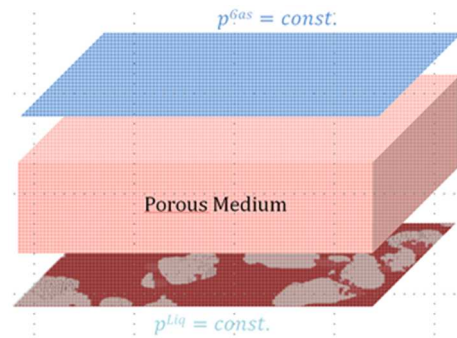


Figure 34: Simulation domain containing the binarized GDL microstructure (rose) in the middle and gas phase pressure boundary condition (blue) on top (channel side). On the bottom (CL side) nano-pores of the MPL are considered as solid (red). Light freckles indicate liquid phase phase inlet through MPL macro-pores.

Definition of solid-fluid and solid-fluid-fluid interactions is of utmost importance to a proper modelling of liquid phase transport through a two-phase system. Since the contact angle defines, if a fluid is wetting ($\theta_c < 90^\circ$) or non-wetting ($\theta_c > 90^\circ$), it has to be chosen thoughtfully. Based on literature the contact angles were chosen as $\theta_c^{Carbon} = 80^\circ$ [24] and $\theta_c^{PTFE} = 115^\circ$ [28] with respect to the liquid phase. By choosing $\theta_c^{PTFE} > 90^\circ$, the binder material is identified as a non-wetting, hydrophobic solid material. It influences two-phase transport locally within the LB model directly via equations (51) and (52) and impedes liquid phase transport in dependence on the PTFE distribution and content.

5.3. Results

Lattice-Boltzmann simulations were conducted for three different loadings, namely 0, 2.5 and 5 wt% of hydrophobic binder inside the porous microstructure of the GDL. Different capillary pressures were imposed in several independent simulations and the systems were equilibrated, resulting in simulation states at varying saturation levels. Whereas the calculation of the saturation levels was straightforward by evaluating the ratio of liquid phase to overall density, the determination of the relative permeability of the gas phase was not that trivial. Assuming, that the relevant liquid phase transport can be considered as single phase plug-flow without any counter-flow of another phase, the liquid phase was (only for the calculation of κ^{gas}) also considered as solid. With the gas phase as the only mobile phase in the system, relative permeabilities were calculated using the Geodict module *FlowDict*.

Figure 35 shows the results, which were derived as described above. The capillary pressure-saturation relationship shows up in form of an S-type curvature, as it was expected. Furthermore it can be seen, that the transition from low to high saturations is shifted towards higher capillary pressures when more PTFE is distributed, owing to the hydrophobic nature of the additive. Figure 35 also shows on the right the dependence of the relative permeability of the gas phase as function of the imposed capillary pressure. From low to intermediate saturations no clear trends are observable, but the delay of the sharp transition towards higher liquid phase saturations appears again in form of an equivalent harsh decrease of the relative permeability. It can be stated therefore, that an increased load of PTFE

retards the event of flooding, i.e., that a saturation level is reached, where the porous structure becomes completely impermeable for the gas phase ($\kappa^{gas} = 0$). The little inset in the right graph of Figure 35 shows the minimum capillary pressure at first occurrence of flooding as function of the PTFE content, this is also just another indication of delayed flooding due to hydrophobic effects.

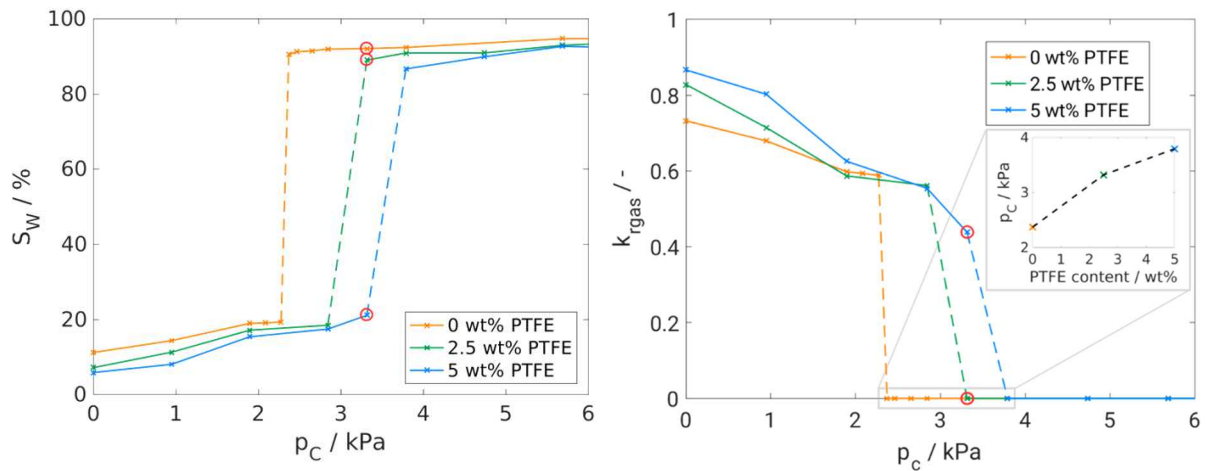


Figure 35: Left: Capillary pressure-saturation curve for three different PTFE loadings. Right: Relative permeability of the gas phase as function of the applied capillary pressure and for three different binder contents. Red markers indicate simulation states, for which 3D representations are shown in Figure 36.

Based on above observations it can be deduced, that the utilized Lattice-Boltzmann model reflects the expected impeding effect of PTFE as hydrophobic binder on the liquid water transport through porous GDL material.

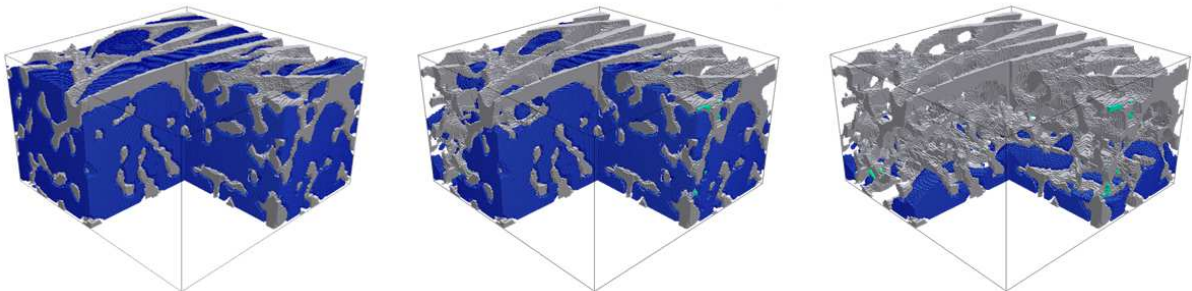


Figure 36: 3D representation of simulation states from partially saturated GDL material for binder contents of 0, 2.5 and 5 wt% PTFE (left to right). Carbon fibers are depicted in grey, whereas liquid phase and binder material are colored in blue and turquoise respectively. The simulation states are marked with red circles in the graphs of Figure 35.



D3.1: Report on models describing the main degradations modes and analysis of their stressing factors



5.4. Conclusions on the GDL degradation model

In order to investigate the effect of PTFE loss in the GDL a Lattice Boltzmann model has been developed which allows simulating the two phase transport in real GDL microstructures obtained from μ CT. The effect of PTFE loading has been studied by varying the amount of PTFE distributed within the simulated domain. Effective transport properties such as capillary pressure-saturation relations and relative permeability have been derived from these simulations. An enhanced flooding of the GDL with reduction of the PTFE content is obtained.

Future simulations will extend this work to include a wider range of capillary pressures and PTFE contents. Furthermore also another simulation approach, where the capillary pressure is linearly ramped over time, will be utilized for a better coverage of data points in the intermediate saturation range. Eventually, the derived PTFE-dependent effective transport properties will be used in the single cell performance models in order to investigate the effect of GDL-degradation on cell performance.



References

- [1] Bhatnagar, P.L., Gross, E.P. and Krook, M. 1954. A Model for Collision Processes in Gases. I. Small Amplitude Processes in Charged and Neutral One-Component Systems. *Physical Review*. 94, 3 (May. 1954), 511–525.
- [2] Chandesris, M., Medeau, V., Guillet, N., Chelghoum, S., Thoby, D. and Fouda-Onana, F. 2015. Membrane degradation in {PEM} water electrolyzer: Numerical modeling and experimental evidence of the influence of temperature and current density. *International Journal of Hydrogen Energy*. 40, 3 (2015), 1353–1366.
- [3] Chandesris, M., Vincent, R., Guetaz, L., Roch, J.-S., Thoby, D. and Quinaud, M. 2017. Membrane degradation in PEM fuel cells: From experimental results to semi-empirical degradation laws. *International Journal of Hydrogen Energy*. 42, 12 (Mar. 2017), 8139–8149.
- [4] Cherevko, S., Keeley, G.P., Geiger, S., Zeradjanin, A.R., Hodnik, N., Kulyk, N. and Mayrhofer, K.J.J. 2015. Dissolution of Platinum in the Operational Range of Fuel Cells. *ChemElectroChem*. 2, 10 (May. 2015), 1471–1478.
- [5] Chopard, B., Dupuis, A., Masselot, A. and Luthi, P. 2002. Cellular Automata and Lattice Boltzmann Techniques: An Approach to Model And Simulate Complex Systems. *Advances in Complex Systems*. 05, 02n03 (Jun. 2002), 103–246.
- [6] Frensch, S.H., Serre, G., Fouda-Onana, F., Jensen, H.C., Christensen, M.L., Araya, S.S. and Kär, S. 2019. Impact of iron and hydrogen peroxide on membrane degradation for polymer electrolyte membrane water electrolysis: Computational and experimental investigation on fluoride emission. *Journal of Power Sources*. 420, (2019), 54–62.
- [7] Futter, G.A., Gazdzicki, P., Friedrich, K.A., Latz, A. and Jahnke, T. 2018. Physical modeling of polymer-electrolyte membrane fuel cells: Understanding water management and impedance spectra. *Journal of Power Sources*. 391, (Jul. 2018), 148–161.
- [8] Futter, G.A., Latz, A. and Jahnke, T. 2019. Physical modeling of chemical membrane degradation in polymer electrolyte membrane fuel cells: Influence of pressure, relative humidity and cell voltage. *Journal of Power Sources*. 410-411, (Jan. 2019), 78–90.
- [9] Gubler, L., Dockheer, S. and Koppenal, H. 2011. Radical (HO, H and HOO) Formation and Ionomer Degradation in Polymer Electrolyte Fuel Cells. *J. Electrochem. Soc.* 158, 7 (2011), B755–B769.
- [10] Harzer, G.S., Schwämmlein, J.N., Damjanovic, A.M., Ghosh, S. and Gasteiger, H.A. 2018. Cathode Loading Impact on Voltage Cycling Induced PEMFC Degradation: A



- Voltage Loss Analysis. *Journal of The Electrochemical Society*. 165, 6 (2018), F3118–F3131.
- [11] LaConti, A.B., Hamdan, M. and McDonald, R.C. 2003. Mechanisms of membrane degradation. A.L. Hubert A. Gasteiger Wolf Vielstich, ed. *Handbook of Fuel Cells – Fundamentals, Technology and Applications*. 647–662.
 - [12] Latva-Kokko, M. and Rothman, D.H. 2005. Static contact angle in lattice Boltzmann models of immiscible fluids. *Physical Review E*. 72, 4 (Oct. 2005).
 - [13] Leclaire, S., Reggio, M. and Trépanier, J.-Y. 2011. Isotropic color gradient for simulating very high-density ratios with a two-phase flow lattice Boltzmann model. *Computers & Fluids*. 48, 1 (Sep. 2011), 98–112.
 - [14] Liu, H., Valocchi, A.J. and Kang, Q. 2012. Three-dimensional lattice Boltzmann model for immiscible two-phase flow simulations. *Physical Review E*. 85, 4 (Apr. 2012).
 - [15] Redmond, E.L., Setzler, B.P., Alamgir, F.M. and Fuller, T.F. 2014. Elucidating the oxide growth mechanism on platinum at the cathode in PEM fuel cells. *Physical Chemistry Chemical Physics*. 16, 11 (2014), 5301.
 - [16] Reis, T. and Phillips, T.N. 2007. Lattice Boltzmann model for simulating immiscible two-phase flows. *Journal of Physics A: Mathematical and Theoretical*. 40, 14 (Mar. 2007), 4033–4053.
 - [17] Robin, C., Gerard, M., d Arbigny, J., Schott, P., Jabbour, L. and Bultel, Y. 2015. Development and experimental validation of a PEM fuel cell 2D-model to study

- heterogeneities effects along large-area cell surface. *Int. J. Hydrogen Energy*. 40, 32 (2015), 10211–10230.
- [18] Rothman, D.H. and Keller, J.M. 1988. Immiscible cellular-automaton fluids. *Journal of Statistical Physics*. 52, 3-4 (Aug. 1988), 1119–1127.
- [19] Sukop, M.C. and Thorne, D.T. 2006. *Lattice Boltzmann Modeling: An Introduction for Geoscientists and Engineers*. Springer Berlin Heidelberg.
- [20] Tölke, J. 2002. Lattice Boltzmann simulations of binary fluid flow through porous media. *Philosophical Transactions of the Royal Society of London. Series A: Mathematical, Physical and Engineering Sciences*. 360, 1792 (Mar. 2002), 535–545.
- [21] Topalov, A.A., Cherevko, S., Zeradjanin, A.R., Meier, J.C., Katsounaros, I. and Mayrhofer, K.J.J. 2014. Towards a comprehensive understanding of platinum dissolution in acidic media. *Chem. Sci*. 5, 2 (2014), 631–638.
- [22] Tsotridis, G., Pilenga, A., Marco, G.D. and Malkow, T. 2015. EU HARMONISED TEST PROTOCOLS FOR PEMFC MEA TESTING IN SINGLE CELL CONFIGURATION FOR AUTOMOTIVE APPLICATIONS. *JRC Science for Policy Report*. (2015).
- [23] Wong, K.H. and Kjeang, E. 2015. Mitigation of Chemical Membrane Degradation in Fuel Cells: Understanding the Effect of Cell Voltage and Iron Ion Redox Cycle. *ChemSusChem*. 8, 6 (2015), 1072–1082.
- [24] Wood, D.L., Rulison, C. and Borup, R.L. 2010. Surface Properties of PEMFC Gas Diffusion Layers. *Journal of The Electrochemical Society*. 157, 2 (2010), B195.
- [25] Zhou, P. and Wu, C.W. 2007. Numerical study on the compression effect of gas diffusion layer on PEMFC performance. *Journal of Power Sources*. 170, (2007), 93–100.
- [26] Zou, Q. and He, X. 1997. On pressure and velocity boundary conditions for the lattice Boltzmann BGK model. *Physics of Fluids*. 9, 6 (Jun. 1997), 1591–1598.
- [27] 2019. *About Geodict*. Math2Market GmbH.
- [28] 2009. *Surface Energy Data For PTFE: Polytetrafluoroethylene*. Diversified Enterprises.